JOURNAL OF SPACECRAFT AND ROCKETS
Vol. 61, No. 5, September–October 2024

Coupled Spacecraft Charging Due to Continuous Electron Beam Emission and Impact

Julian Hammerl* and Hanspeter Schaub†
University of Colorado Boulder, Boulder, Colorado 80303

https://doi.org/10.2514/1.A36010

Spacecraft charge naturally in orbit due to the plasma environment and the electromagnetic radiation from the sun. By emitting an electron beam, a servicer spacecraft can control its electric potential and also the potential of a neighboring target if the electron beam is aimed at the target spacecraft. In addition, the impacting electron beam excites secondary electrons and x-rays, providing a way to touchlessly sense the potential of the target. Because of the electron beam, the charging dynamics of the two spacecraft are coupled. This paper studies the effects of the beam on the electric potentials using a numerical charging model. It is found that multiple equilibria may exist due to the electron beam. Jumps between equilibrium configurations are possible when the electron beam energy is quickly reduced or when current fluctuations are present. Being aware of multiple equilibrium configurations is important for feedback-based charge control but also enables a new open-loop charge control around one of the equilibria. The effect of the electron beam on the spacecraft potentials is studied for geostationary Earth orbit and cislunar space. It is found that the current applied by the beam to the target may influence remote electric potential sensing methods.

Downloaded by Univ of Colorado Libraries - Boulder on October 8, 2024 | http://arc.aiaa.org | DOI: 10.2514/1.A36010

I. Introduction

SPACECRAFT build up electrostatic charge in the space environment, which affects spaceflight in various ways. Arcing can occur between spacecraft components if the spacecraft is not fully conducting and some parts are charged to significantly different electric potentials, referred to as differential charging. This can reduce the lifetime of a solar panel if arcing occurs on the panel [1,2]. Two nearby spacecraft can also be subject to electrostatic discharges if they are charged to different potentials and are very close to each other, for example, during docking. Additionally, two charged spacecraft in close proximity exert electrostatic forces on each other if the electric potentials are high enough. These forces can affect rendezvous and proximity operations [3] but can also be used for active debris removal [4,5]. Natural charging events were recorded by the Applied Technology Satellite 6 (ATS-6), with potentials reaching–19 kV during eclipse in geostationary Earth orbit (GEO) [6].

Spacecraft charging has been extensively reviewed in Ref. [7] and studied with emphasis on, among other topics, mitigation of charging [8], modeling of spacecraft charging [9], detection of discharging events [10], and characterization of the secondary electron yield [11] that plays an important role in spacecraft charging. Charging levels in various orbital regions have been investigated, such as low Earth orbit (LEO) [12], GEO [13], and cislunar space [14]. However, most research on spacecraft charging focuses on the effects of only the space environment, that is, how much a spacecraft charges naturally due to the ambient plasma environment. Charging induced by electron beam impact, electron beam emission, and ion beam emission is discussed relatively briefly in Chapters 9-12 of Ref. [7]. The coupled charging behavior of two spacecraft in close proximity, where one spacecraft emits an electron beam that hits the other spacecraft, has been studied for the application of the electrostatic tractor active debris removal method [15–18]. These papers specifically study the effect of the charging levels on the electrostatic force magnitude between the two spacecraft, with the goal of improving the performance of the electrostatic tractor, as a higher force magnitude leads to a reduction of the time required to reorbit retired satellites from GEO to a graveyard orbit. The motivation of this paper, however, is to study the coupled effect of electron emission and impact on the transients of the servicer and target spacecraft potentials, as well as the influence of the beam on remote sensing methods that estimate the electric potential of another spacecraft.

Remotely sensing the electric potential of a nearby spacecraft is valuable for spaceflight as it provides a warning for probable electric discharges during docking, reduces the control effort during rendezvous and proximity operations for charged spacecraft [3,19], and increases the safety of the electrostatic tractor debris removal process [20]. Two promising remote electric potential sensing methods have been proposed: the electron method [21] and the x-ray method [22]. Both methods use an electron gun that is attached to a servicing satellite. The electron gun is aimed at a target object and excites secondary electrons and x-rays from the target, as illustrated in Fig. 1. The secondary electrons are released from the surface of the target with negligible kinetic energy. If the target is charged negatively and the servicer is charged positively, the secondary electrons are repelled from the target and accelerated toward the servicer. This is generally the case as spacecraft naturally charge to negative potentials in eclipse, while the servicing satellite is charged positively due to the electron beam emission. The increase in kinetic energy of the secondary electrons as they travel from the target to the servicer equals the electric potential difference between the target and the servicer. Thus, by determining the potential of the servicer with a Langmuir probe [23] and measuring the kinetic energy of the secondary electrons with a retarding potential analyzer (RPA), one can estimate the electric potential of the target object [21]. This is referred to as the electron method. Note that the potential of the servicer can also be measured with a RPA [24]. The x-rays that are excited by the electron beam are emitted with an energy up to the kinetic energy of the beam electrons as they impact the target object (called the effective energy or landing energy). If the two spacecraft are charged, the electron beam is accelerated or decelerated as it travels from the servicer to the target, depending on the relative potential between the two craft. The difference between the initial kinetic energy of the beam and the landing energy corresponds to the electric potential difference between the two spacecraft. The initial energy of the electron beam is known as it corresponds to the operating energy of the electron gun. By using an x-ray detector on the servicing craft and finding the maximum x-ray energy in the recorded x-ray spectrum, one can infer the electric potential of the target object if the potential of the servicer is known. This is the x-ray method. Both methods have been validated experimentally [25,26] for terrestrial

Received 1 February 2024; revision received 8 May 2024; accepted for publication 28 May 2024; published online 28 June 2024. Copyright © 2024 by the authors. Published by the American Institute of Aeronautics and Astronautics, Inc., with permission. All requests for copying and permission to reprint should be submitted to CCC at www.copyright.com; employ the eISSN 1533-6794 to initiate your request. See also AIAA Rights and Permissions www.aiaa.org/randp.

*Graduate Research Assistant, Ann and H.J. Smead Department of Aerospace Engineering Sciences; julian.hammerl@colorado.edu. Student Member AIAA.

†Department Chair, Ann and H.J. Smead Department of Aerospace Engineering Sciences. Fellow AIAA.

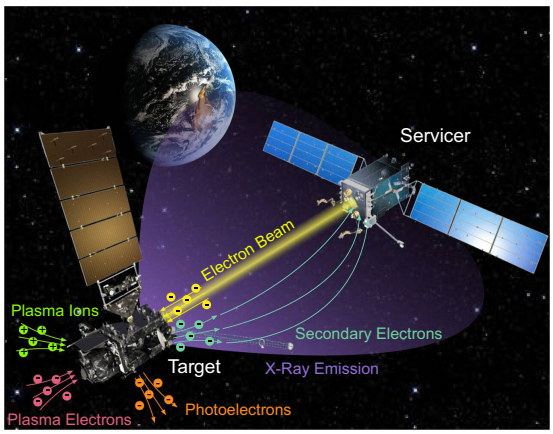

Fig. 1 Illustration of spacecraft charging and electric potential sensing.

conditions in the Electrostatic Charging Laboratory for Interactions Between Plasma and Spacecraft (ECLIPS) vacuum chamber [27].

One key aspect of these remote sensing methods that has been ignored in prior theoretical and experimental work is the effect of the electron beam on the electric potential of the target. The electrons from the beam impose a negative current on the target object, which changes the equilibrium potential within a second, depending on the capacitance of the spacecraft. One might be interested in the natural potential of the object, that is, the potential resulting from the space environment without the influence of the electron beam. Therefore, any impact of the electron beam on the potential must be minimized; otherwise, the potential being measured does not correspond to the natural potential. To what extent the electric potential is affected by the electron beam depends on the conditions of the space environment and the electron beam parameters, i.e., the beam current and beam energy. The electron beam current and energy can be chosen such that the electron beam does not change the target potential significantly; however, the remote sensing methods impose restrictions on the beam parameters in order to generate a sufficient amount of secondary electrons and x-rays. For example, both methods benefit from a high electron beam current as this increases the emission of secondary electrons and x-rays. A low beam energy is preferred for the electron method because the secondary electron yield (the number of secondaries generated per incident electron), although relatively uncertain and dependent on many factors [11], is generally the highest for landing energies less than 2–3 keV. For the x-ray method, a high landing energy is favorable. The energy-dependent efficiency curve[‡] of the x-ray detector used in prior work [26–28] is the highest for landing energies between 5 and 10 keV. X-rays also allow for material determination [22], as characteristic x-rays are emitted with an energy specific to an element [29]. If the x-rays are simultaneously used for material identification, even higher landing energies are preferred such that characteristic x-ray peaks beyond 5–10 keV are visible in the recorded x-ray spectrum. In prior experimental work on the two sensing methods [25,26,28,30], the potential of the target object was held constant during the experiments using high-voltage power supplies, so the effect of the negative current due to the electron beam on the electric potential of the target was eliminated. It should be noted that a passive x-ray method for electric potential estimation has been investigated [31] and employs the x-rays generated by the ambient plasma electrons, without using an active electron beam. Thus, there is no external current due to the electron beam that disturbs the equilibrium potential of the target object. The drawback of the passive x-ray method is that it requires knowledge of the energy distribution of the local electron population and is based on theoretical x-ray models that are material dependent and only approximate.

This paper numerically investigates the coupled charging behavior of a servicing and target spacecraft due to the emission of an electron beam from the servicer and the impact of the beam on the target. Analytical spacecraft charging models are employed that assume a Maxwellian plasma distribution and spherical spacecraft. Multiple equilibria are found to exist due to the electron-beam-induced current and due to secondary electron emission from the target. The requirements for the existence of multiple equilibria are presented, and the regions of convergence for these equilibria are studied. The goal of this paper is to investigate what can cause a jump from one equilibrium configuration to another as well as to investigate potential applications that use the existence of multiple equilibria. In addition, this paper aims at studying the effect of the electron beam current on remote electric potential sensing methods. An overview of the spacecraft charging model used in this work is provided in Sec. II.B. The possibility and significance of multiple equilibria as well as spacecraft charging transients are discussed in Sec. III. Section IV investigates the effects of the electron beam on remote electric potential sensing methods for the GEO regime as well as lunar orbit.

II. Background

Spacecraft charge due to various electric currents in the space environment. The ambient plasma in space contains charged particles such as energetic electrons and ions. When these particles impact on the surface of a spacecraft, they transfer their charge to the spacecraft, resulting in what is referred to as the electron and ion plasma currents (see Ref. [7] chap. 1). When electrons and ions impact on a surface, they transfer their energy to neighboring electrons in the material. If enough energy is transferred, one or more *secondary* electrons leave the surface material with low energies of a few electron volts. This is referred to as secondary electron emission (see Ref. [7] chap. 3, and Ref. [32] chap. 8). It is also possible that an incident electron is backscattered and leaves the surface material again, resulting in backscattered electron emission (see Ref. [7] chap. 3). In contrast to the secondary electron emission, the emitted electron is the same as the incident electron, so the probability of generating a backscattered electron cannot exceed unity. In sunlight, the incoming electromagnetic radiation from the sun excites photoelectrons from the surface of a spacecraft. These electrons are repelled if the spacecraft is charged negatively, leading to a positive photoelectric current (see Ref. [7] chap. 7). In addition to these naturally occurring currents, the electron beam that is used for the electric potential sensing methods described previously imposes an artificial current. This current is negative for the target object due to the collection of negative charge (see Ref. [7] chap. 9) and positive for the servicing satellite due to the emission of electrons (see Ref. [7] chap. 10). The electron beam impacting on the target also generates secondary and backscattered electrons.

A. Spacecraft Charging Model

A similar charging model as in Ref. [15] is applied. This model assumes spherical, fully conducting spacecraft. Thus, all charging occurs on the surface, and the spacecraft has only one electric potential ϕ. A single-Maxwellian plasma distribution is assumed. The radii of the spherical servicer and target spacecraft are set to $R_S = R_T = 1$ m. The plasma electron current is modeled as (see Ref. [33] chap. 4)

$$I_e(\phi) = \begin{cases} -\dfrac{A_p q n_e w_e}{4} e^{\phi/T_e} & \text{if } \phi \leq 0 \\ -\dfrac{A_p q n_e w_e}{4}\left(1 + \dfrac{\phi}{T_e}\right) & \text{if } \phi > 0 \end{cases} \tag{1}$$

where A_p is the surface area of the spacecraft exposed to the plasma, q is the elementary charge, and n_e and T_e are the electron density in units of m^{-3} and electron temperature in units of electron volts of the plasma, respectively. The (three-dimensional) thermal electron velocity is equal to $w_e = \sqrt{8T_e/(m_e\pi)}$, with electron mass m_e. For a spherical spacecraft with radius R, the plasma exposed area equals

[‡]Data available online at https://www.amptek.com/products/x-ray-detectors/sipin-x-ray-detectors/sipin-x-ray-detectors [retrieved 25 June 2024].

Downloaded by Univ of Colorado Libraries - Boulder on October 8, 2024 | http://arc.aiaa.org | DOI: 10.2514/1.A36010

$A_p = 4\pi R^2$. The plasma electron current is negative due to the negative charge of electrons. A negatively charged ($\phi < 0$) spacecraft repels electrons, resulting in a low current, while a positively charged spacecraft results in a high electron current due to the attraction of electrons.

Similarly to the electron current, the plasma ion current is approximated by (see Ref. [33] chap. 4):

$$I_i(\phi) = \begin{cases} \frac{A_p q n_i w_i}{4}\left(1 - \frac{\phi}{T_i}\right) & \text{if } w_i \geq v_{i,\text{bulk}}, \quad \phi \leq 0 \\ \frac{A_p q n_i w_i}{4} e^{-\phi/T_i} & \text{if } w_i \geq v_{i,\text{bulk}}, \quad \phi > 0 \\ A_{\text{ram}} q n_i v_{i,\text{bulk}} & \text{if } w_i < v_{i,\text{bulk}} \end{cases} \tag{2}$$

The variables are similar as what was previously mentioned, but the subscript i (ions) replaces the subscript e (electrons). Additionally, the mesothermal case is considered when the bulk velocity $v_{i,\text{bulk}}$ of the ions (the average, directional velocity of the ion flow) with respect to the spacecraft is greater than the thermal velocity w_i of the ions. In this case, the ions only impact on the ram side of the spacecraft with area A_{ram}, and the resulting current does not depend on the spacecraft potential. For the spherical spacecraft that is assumed in this work, $A_{\text{ram}} = R^2\pi$. In LEO, the mesothermal case ($w_i < v_{i,\text{bulk}}$) applies due to the low ion energies (less than 1 eV) and high orbital velocities. In GEO, ions are more energetic (order of kilo-electron-volts), so the thermal ion velocity dominates ($w_i > v_{i,\text{bulk}}$). In cislunar space, it depends on the location of the Moon, as the Moon can be inside or outside of Earth's magnetosphere and in the solar wind (Sec. IV.B). The charging code implemented for this work automatically compares the ion thermal velocity w_i to a specified ion bulk velocity $v_{i,\text{bulk}}$. It is assumed that the ion species consists of solely hydrogen ions (H^+). Thus, for the thermal ion velocity $w_i = \sqrt{8T_i/(m_i\pi)}$, it is assumed that the ion mass m_i equals the mass of a proton m_p. This is a valid assumption for geostationary orbit, as hydrogen is the dominant ion species in the magnetosphere with relative abundances of about 80% in GEO during low geomagnetic activity [34]. During high solar activity (planetary index $K_p \geq 4$), ionospheric outflow is enhanced, which delivers additional plasma [especially oxygen ions (O^+)] to higher altitudes, resulting in relative H^+ and O^+ abundances in GEO of about 50% each [34]. Depending on the location of the Moon with respect to Earth, the Moon is either inside Earth's magnetosphere (H^+ dominated) or outside in the solar wind. The solar wind primarily consists of about 95% electrons and protons and 4% helium nuclei (see Ref. [32] chap. 3). Thus, the assumption that the ion species consists of solely protons is also justified for cislunar space.

The secondary electron and backscattered electron emission current due to plasma electron impact is calculated by

$$I_{\text{SEE},B,e}(\phi) = \begin{cases} -<Y_{\text{SEE},B,e}> \cdot I_e(\phi) & \text{if } \phi \leq 0 \\ -<Y_{\text{SEE},B,e}> \cdot I_e(\phi) e^{-\phi/T_{\text{SEE}}} & \text{if } \phi > 0 \end{cases} \tag{3}$$

and the secondary electron emission due to plasma ion impact is computed as

$$I_{\text{SEE},i}(\phi) = \begin{cases} <Y_{\text{SEE},i}> \cdot I_i(\phi) & \text{if } \phi \leq 0 \\ <Y_{\text{SEE},i}> \cdot I_i(\phi) e^{-\phi/T_{\text{SEE}}} & \text{if } \phi > 0 \end{cases} \tag{4}$$

The two cases are needed due to the fact that secondary electrons are emitted with very low energy, so the resulting current drops off quickly with increasing positive spacecraft potential ($T_{\text{SEE}} = 5$ eV in this work) as the negatively charged secondary electrons are attracted back to a positively charged spacecraft. The mean yield over all particle energies $<Y>$ is computed by

$$<Y> = \frac{\int_L^\infty Y(E)(E/(E \pm \phi))F(E \pm \phi)\mathrm{d}E}{\int_L^\infty (E/(E \pm \phi))F(E \pm \phi)\mathrm{d}E} \tag{5}$$

where $Y(E)$ is a placeholder for the corresponding yield: secondary electron yield due to electron impact Y_{SEE}, backscattered electron yield Y_B, combined electron yield $Y_{\text{SEE},B} = Y_{\text{SEE}} + Y_B$, or secondary electron yield due to ion impact $Y_{\text{SEE},i}$. The energy of the incoming particle is denoted by E, and the particle flux distribution $F(E)$ (for electrons or ions) is given by [35]

$$F(E) = \sqrt{\frac{q_0}{2\pi T m}}\frac{E}{T} n \exp\left(-\frac{E}{T}\right) \tag{6}$$

for a Maxwellian plasma with plasma temperature T (measured in electron volts) and plasma density n. In Eq. (5), the positive sign of $\pm$ applies to ions and the negative sign to electrons. The lower bound L of the integral is 0 for the repelled particles (e.g., for electrons if $\phi < 0$) and $|\phi|$ for the attracted particles, and the upper bound is set as 1 MeV in this work. In the mesothermal case of Eq. (2), the mean ion-induced secondary electron yield is simply $<Y_{\text{SEE},i}> = Y_{\text{SEE},i}(E)$, with $E = (1/2)m_i v_{i,\text{bulk}}^2$ in units of electron volts.

The secondary electron and backscattered electron yield $Y_{\text{SEE},B,e}$ is the average number of secondary and backscattered electrons generated per incident electron and is approximated using the analytical model from Ref. [36],

$$Y_{\text{SEE},B}(E) = 4 \cdot Y_{\max} \frac{E/E_{\max}}{(1 + E/E_{\max})^2} \tag{7}$$

where E is the landing (effective) energy of the incident electron when it impacts on the surface, $Y_{\max}$ is the maximum electron yield, and $E_{\max}$ is the landing energy at which this maximum occurs. If the electron comes from an electron beam emitted from a servicer, rather than from the ambient plasma environment, the landing energy is computed as

$$E = E_{\text{EB}} - \phi_S + \phi_T \tag{8}$$

Note that the electron yield is relatively uncertain as it depends on many factors such as surface material, roughness, and level of oxidation, and it changes after prolonged exposure to the space environment [11]. The yield for isotropic flux is assumed to be double the yield for normal incidence [35,36]. Assuming a spacecraft made of aluminum, values of $Y_{\max} = 0.97$ and $E_{\max} = 300$ eV for normal incidence are used in this work (see Ref. [7] chap. 3).

Secondary electrons can also be excited by incoming ions. The corresponding yield is modeled by [35]

$$Y_{\text{SEE},i}(E) = \frac{\beta E^{1/2}}{1 + E/E_{\max,i}} \tag{9}$$

where E is the energy of the incident ion in keV, $E_{\max,i}$ is the energy of the maximum yield, β is a scaling parameter. Similarly to the electron-induced secondary electron emission, the parameters for the electron yield due to incident ions are not well known, and the yield for isotropic flux is assumed to be double the yield for normal incidence [35,36]. For aluminum, the energy that produces the maximum electron yield is assumed to be $E_{\max,i} = 230$ keV, and a yield of $\beta = 0.244$ for 1 keV normally incident protons as extrapolated from data taken at energies greater than 10 keV is used.

The photoelectric current from solar radiation for normal photon incidence is (see Ref. [7] chap. 7)

$$I_{\text{ph}}(\phi) = \begin{cases} j_{\text{ph},0} A_{\text{ph}} & \text{if } \phi \leq 0 \\ j_{\text{ph},0} A_{\text{ph}} e^{-\phi/T_{\text{ph}}} & \text{if } \phi > 0 \end{cases} \tag{10}$$

where $A_{\text{ph}} = R^2\pi$ is the cross-section of the spherical spacecraft that is in sunlight and $j_{\text{ph},0}$ and T_{ph} are the flux and temperature of the emitted photoelectrons, respectively. The flux $j_{\text{ph},0}$ is in the order of 10 $\mu\text{A/m}^2$ but depends on the surface material and can vary with solar activity by a factor of up to 8 [37]. Similarly as with the secondary electron emission, photoelectrons are released with very

Downloaded by Univ of Colorado Libraries - Boulder on October 8, 2024 | http://arc.aiaa.org | DOI: 10.2514/1.A36010

Downloaded by Univ of Colorado Libraries - Boulder on October 8, 2024 | http://arc.aiaa.org | DOI: 10.2514/1.A36010

low energy, requiring an equation with exponential dropoff for positive potentials. In this work, values of $j_{\mathrm{ph},0} = 20\ \mu\mathrm{A/m}^2$ and $T_{\mathrm{ph}} = 2$ eV are used [15]. The electron beam current is modeled as

$$I_{\mathrm{EB},T}(\phi_T, \phi_S) = \begin{cases} -\alpha I_{\mathrm{EB}}(1 - e^{-(E_{\mathrm{EB}}-\phi_S+\phi_T)/T_{\mathrm{EB}}}) & \text{if } E_{\mathrm{EB}} > \phi_S - \phi_T \\ 0 & \text{if } E_{\mathrm{EB}} \leq \phi_S - \phi_T \end{cases} \tag{11}$$

for the target spacecraft, where I_{EB} and E_{EB} are the electron gun current and operating energy (i.e., the kinetic energy of the electrons as they exit the electron gun) and ϕ_T and ϕ_S denote the electric potential of the target and the servicer, respectively. Because of the deflection and expansion of the electron beam [38], only a fraction α of the electrons emitted from the gun might reach the target. For simplicity, however, $\alpha = 1$ is assumed in this work. The electron beam electrons can only reach the target if the beam energy E_{EB} is greater than the electric potential difference between the two craft, $\phi_S - \phi_T$. Otherwise, the electrons do not reach the target, and the net current due to the electron beam is approximately zero. In contrast to prior work [15,17,39], where the beam current is modeled as being equal to $-\alpha I_{\mathrm{EB}}$ if $E_{\mathrm{EB}} > \phi_S - \phi_T$ and zero if $E_{\mathrm{EB}} \leq \phi_S - \phi_T$, an exponential dropoff is used here with $T_{\mathrm{EB}} = 20$ eV. This removes the discontinuity at $E_{\mathrm{EB}} = \phi_S - \phi_T$, which benefits numerical root finding of the equilibrium potential and the propagation of the charging dynamics with numerical methods.

The combined secondary and backscattered electron current emitted from the target object due to the electron beam impact is equal to

$$I_{\mathrm{SEE},B,\mathrm{eb}}(\phi_T, \phi_S) = \begin{cases} -Y_{\mathrm{SEE},B}(E) \cdot I_{\mathrm{EB},T} & \text{if } \phi_T < 0 \\ -Y_{\mathrm{SEE},B}(E) \cdot I_{\mathrm{EB},T} e^{-\phi/T_{\mathrm{SEE}}} & \text{if } \phi_T \geq 0 \end{cases} \tag{12}$$

Similarly to the electron beam current on the target, the electron beam current on the servicer is modeled as

$$I_{\mathrm{EB},S}(\phi_T, \phi_S) = \begin{cases} I_{\mathrm{EB}}(1 - e^{-(E_{\mathrm{EB}}-\phi_S+\phi_T)/T_{\mathrm{EB}}}) & \text{if } E_{\mathrm{EB}} > \phi_S - \phi_T \\ 0 & \text{if } E_{\mathrm{EB}} \leq \phi_S - \phi_T \end{cases} \tag{13}$$

Using all the mentioned currents, the total current is

$$\begin{aligned} I_{\mathrm{tot},S}(\phi_T, \phi_S) = {} & I_e(\phi_S) + I_i(\phi_S) + I_{\mathrm{ph}}(\phi_S) + I_{\mathrm{SEE},B,e}(\phi_S) \\ & + I_{\mathrm{SEE},i}(\phi_S) + I_{\mathrm{EB},S}(\phi_T, \phi_S) \end{aligned} \tag{14}$$

for the servicing satellite and

$$\begin{aligned} I_{\mathrm{tot},T}(\phi_T, \phi_S) = {} & I_e(\phi_T) + I_i(\phi_T) + I_{\mathrm{ph}}(\phi_T) + I_{\mathrm{SEE},B,e}(\phi_T) \\ & + I_{\mathrm{SEE},i}(\phi_T) + I_{\mathrm{EB},T}(\phi_T, \phi_S) + I_{\mathrm{SEE},B,\mathrm{eb}}(\phi_T, \phi_S) \end{aligned} \tag{15}$$

for the target spacecraft.

To achieve an equilibrium potential, the total current on each spacecraft must be zero. Thus, the equilibrium potential of the spacecraft is found by setting Eqs. (14) and (15) equal to zero. No analytical solution exists, so this is solved numerically. In this work, the potential of the servicer is computed first. Knowing the servicer potential, the potential of the target is then determined by finding the root of Eq. (15). The natural potential of a spacecraft is found by setting the electron beam current equal to zero, $I_{\mathrm{EB}} = 0\ \mu$A.

Note that the electron beam current depends on the potential of both the target and the servicer. As mentioned previously, for two-craft formations, the servicer potential is computed before the target potential within this work. When the servicer potential is computed, knowledge of the target potential is required to determine whether or not the beam is coming back to the servicer, resulting in a net zero electron beam current on the servicer. However, because the target potential is unknown at this point, the assumption is made that only the servicer potential determines whether or not the beam is coming back to the servicer. That is, it is assumed that $\phi_T = 0$ when computing the servicer equilibrium potential. This assumption is discussed and justified in the next subsection.

It is assumed that the only coupling between the servicer and the target is due to the electron beam. A highly charged spacecraft perturbs the plasma distribution in its vicinity, which affects the plasma electron and ion current collected by a neighboring spacecraft. Additionally, secondary electrons and photoelectrons emitted from the negatively charged target may be accelerated to the positively charged servicer. Such interactions and effects of the electric fields of the satellites on each other are neglected in this work, but recommended for future studies.

The electric potential is propagated over time using the differential equations

$$\dot{\phi}_S = \frac{1}{C_S} \cdot I_{\mathrm{tot},S}(\phi_T, \phi_S) \tag{16a}$$

$$\dot{\phi}_T = \frac{1}{C_T} \cdot I_{\mathrm{tot},T}(\phi_T, \phi_S) \tag{16b}$$

where C is the capacitance of the spacecraft and is equal to $C = 4\pi\epsilon_0 R$ for a spherical spacecraft with radius R, with ϵ_0 being the vacuum permittivity. For propagations over time, the potential of the target is known from the previous time step, so the $\phi_T = 0$ assumption is not used when computing the servicer currents. That is, the total current on the servicer and target are computed simultaneously for dynamic simulations, as opposed to sequentially (first for the servicer and then for the target) for the determination of equilibrium potentials.

B. Justification of Electron Beam Assumptions

In Eq. (13), it is assumed that the presence of a charged target spacecraft does not affect whether or not the electron beam comes back to the servicing spacecraft. The benefit of this assumption is that the equilibrium electric potentials of the servicer and target can be computed sequentially by finding the root of Eq. (14) and then the root of Eq. (15). Alternatively, without this assumption, the equilibrium potentials could be computed either simultaneously by solving a bivariate root-finding problem for ϕ_S and ϕ_T or by repeatedly finding the equilibrium potentials sequentially in a loop and using the knowledge of one potential to find the other until both solutions have converged. Both of these approaches come with increased complexity and computational effort. Because the charging model discussed in Sec. II.A is approximate and to be used for the rapid computation of electric potentials, forces, and torques, it is desired to keep computational effort low, as long as the assumptions are valid.

To validate the assumption, several simulations are performed with the particle tracing simulation framework SIMION.[§] SIMION computes the electrostatic field by solving Laplace's equation and then propagates the particle trajectories using Newton's second law. The SIMION model does not account for space-charge effects, so the expansion of the electron beam and the effect of the electron beam on the electric field are neglected. Reference [38] shows that the trajectory of the beam center depends only very weakly on beam expansion. Because the main purpose of the SIMION model in this work is to simulate the beam landing area, the implemented model is considered sufficiently accurate, and computationally more expensive models such as particle in cell are not considered.

A total number of 5292 SIMION simulations are run with electron beam energies of $E_{\mathrm{EB}} = 10, 20, 30$ keV; target potentials ϕ_T between −30 and 0 kV with steps of 5 kV; servicer potentials ϕ_S between 0 and 30 kV with steps of 5 kV; separation distances of 15, 20, and 30 m; and 12 different target orientations. The number of beam electrons that hit the target and servicer is recorded. The SIMION simulation setup is shown in Fig. 2. On the left, the entire

[§]Data available online at https://simion.com [retrieved 25 June 2024].

Downloaded by Univ of Colorado Libraries - Boulder on October 8, 2024 | http://arc.aiaa.org | DOI: 10.2514/1.A36010

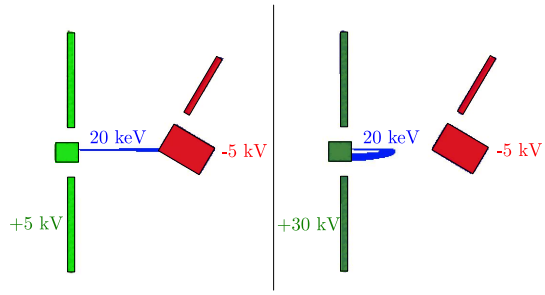

Fig. 2 SIMION simulation.

beam hits the target for a beam energy of $E_{\mathrm{EB}} = 20$ keV, target potential $\phi_T = -5$ kV, servicer potential $\phi_S = 5$ kV, separation distance of 15 m, and target angle of 120 deg. On the right, the entire beam comes back to the servicer for a target potential $\phi_T = -5$ kV, servicer potential $\phi_S = 30$ kV, and the remaining parameters being the same as on the left.

Figure 3 shows the percentage of the beam electrons that come back and hit the servicer as a function of target and servicer potential, for a beam energy of $E_{\mathrm{EB}} = 20$ keV. In the figure, the average percent of servicer hits across all separation distances and target orientations is shown. The solid red line represents $\phi_S = \phi_T + E_{\mathrm{EB}}$. For points below this line, the electron beam is energetic enough to reach the target; see Eq. (11). Note that, depending on the initial direction of the beam, the beam can come back to the servicer despite being energetic enough to reach the target. However, because the beam is aimed at the target in the simulations, the entire beam should hit the target, and no beam electrons are expected to hit the servicer. For points above the solid red line, the beam is not energetic enough to reach the target. When the potential of the servicer ϕ_S is computed, the potential of the target ϕ_T is undetermined, so this line is also unknown.

The dashed red line represents $\phi_S = E_{\mathrm{EB}}$. This line is known when the potential of the servicer is computed. In Eq. (13), it is assumed that only the servicer potential influences whether or not the beam comes back to the servicer. If $\phi_S < E_{\mathrm{EB}}$, the entire beam is assumed to leave the servicer, and if $\phi_S \geq E_{\mathrm{EB}}$, the entire beam is assumed to come back to the servicer, resulting in a net zero current due to the electron beam. For this assumption to hold, the percentage of servicer hits in Fig. 3 must be 100% above the dashed red line and 0% below this line. As can be seen in the figure, this is true for most potential combinations. The percentage of servicer hits is close to 0% below the dashed red line and close to 100% above it. The main discrepancy occurs at the edge case $\phi_S = E_{\mathrm{EB}}$. Given that the average percentage of servicer hits is close to the expected value, the assumption in Eq. (13) is considered justified.

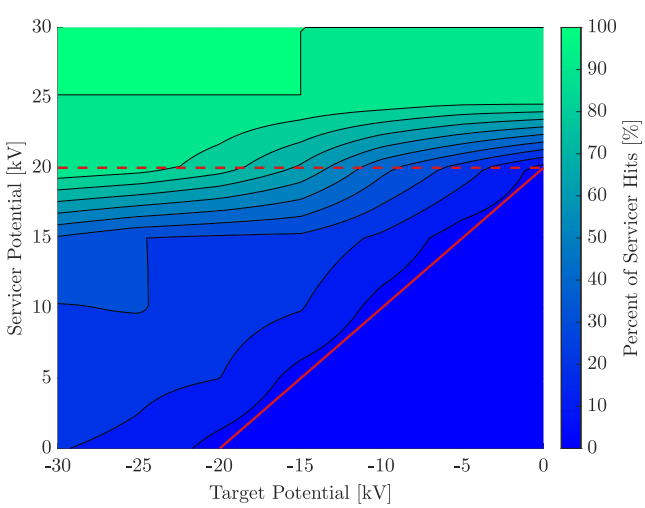

Fig. 3 Percentage of electron beam that hits the servicer for a beam energy of 20 keV. Solid red line: $\phi_S = \phi_T + E_{\mathrm{EB}}$. Dashed red line: $\phi_S = E_{\mathrm{EB}}$.

C. Beam Parameters: Current and Energy

In Chapter 11 of Ref. [7], spacecraft charging due to electron beam emission is figuratively compared to digging a hole. To dig a deeper hole, the amount of dirt thrown out of the hole must exceed the amount of dirt that falls into the hole. However, once the hole is as deep as one can throw, all the dirt that is attempted to be thrown out falls back into the hole. That is, the initial kinetic energy of the dirt is not high enough to overcome the gravitational potential difference between the top and bottom of the hole, and the maximum depth of the hole is reached. Similarly, for a spacecraft that emits an electron beam, the outgoing electron beam current must be greater than the incoming currents. Because negatively charged electrons are emitted, the electron beam current on the servicer is positive and must exceed the negative currents acting on the servicer in order to charge positively. The physical limit on how much the servicer can charge depends on the electron beam energy. Because the servicer charges positively, the emitted electrons are attracted back to the servicer. Once the electric potential of the servicer is as high as the beam energy, the electron beam electrons are unable to escape and come back to the servicer, resulting in a net zero electron beam current. In contrast to the simplified analogy of digging a hole with a constant amount of dirt going in and out of the hole, however, the final electric potential depends not only on the electron beam energy but also on the electron beam current. As the servicer charges positively, more electrons from the ambient plasma environment are attracted to the servicer. That is, the incoming currents increase, and a higher electron beam current is required to charge more positively. Without a higher electron beam current, the servicer cannot charge to the physical limit determined by the beam energy. The presence of another charged spacecraft, in this case the target spacecraft, affects the charging limits. The initial beam energy must be high enough to overcome the electric potential difference between the servicer and the target to ensure that the beam can reach the target and is not coming back to the servicer.

For a spacecraft that is irradiated by an electron beam, the secondary electron yield of the surface material plays an important role. As electrons impact on the surface, secondary electrons are excited that leave the material. If the spacecraft is charged negative, these secondary electrons are repelled by the spacecraft, resulting in a positive current due to the loss of negatively charged electrons. In a similar fashion, incoming electrons can also be backscattered, when the same electron enters and exits the surface material. The average number of secondary electrons generated per incoming electron depends on the effective energy of the incoming electron and is characterized by the secondary electron yield. The effective energy, also called landing energy or impact energy, is the kinetic energy of the incoming electron as it impacts on the surface. For some materials and effective energies, the secondary electron yield can exceed unity. This leads to the interesting charging behavior where an object is charged positively, despite being irradiated with negatively charged electrons. Note that secondary electrons and backscattered electrons are different and can be modeled with two separate yield curves (the secondary electron yield and backscattered electron yield). Both are relatively uncertain and can change after long exposure to the space environment [11]. In this work, both yield curves are modeled combined with the model presented in Ref. [36], and the resulting combined yield is generally referred to here as secondary electron yield.

The photoelectric current and secondary electron currents induced by the ambient plasma electrons and ions as well as by the incoming electron beam are all excited from the surface with low kinetic energies. Thus, all of these currents are strong for a negatively charged spacecraft that repels the released electrons but quickly drop to zero if the spacecraft is charged positively. This drop of current at about 0 V is clearly visible in Fig. 4, in which the various currents from Sec. II.A are shown as a function of the target potential. For this figure, an electron beam current of 50 μA and energy of 20 keV are used, resulting in a servicer potential of about +4.5 kV. Because of the relatively strong photoelectric current of over 60 μA, the equilibrium potential of the target is about 0 V (marked by the black circle).

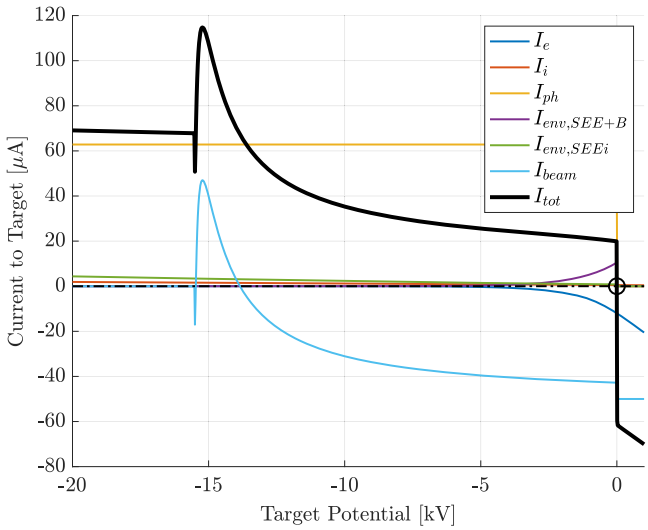

Fig. 4 Currents vs potential of target. $I_{\mathrm{EB}} = 50\ \mu$A, $E_{\mathrm{EB}} = 20$ keV, resulting servicer equilibrium potential of about +4.5 keV.

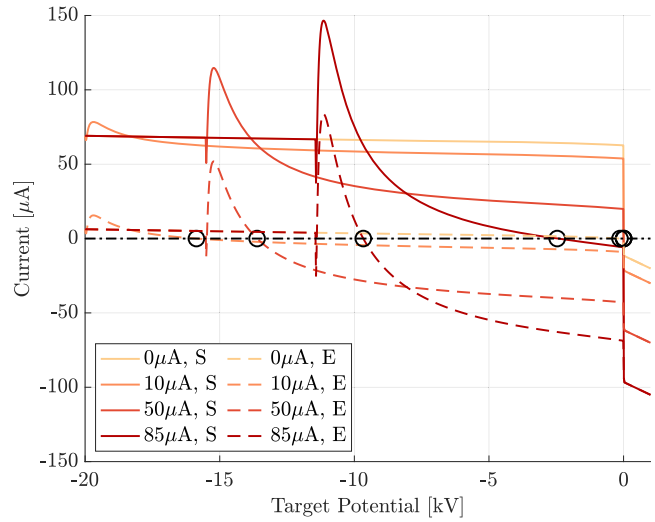

Fig. 5 Current vs potential of target for various beam parameters. $E_{\mathrm{EB}} = 20$ keV.

Examining the total current (black line in Fig. 4) acting on the target as a function of the target potential helps to build understanding of electron-beam-induced spacecraft charging. Starting at the left side of the figure, the electron beam is not energetic enough to reach the target, so the net electron beam current is zero, and the photoelectric current and plasma ion current dominate. Given the servicer equilibrium potential of about +4.5 kV and the initial beam energy of 20 keV, the beam is energetic enough to reach the target for target potentials less negative than −15.5 kV. The total current quickly decreases by the intensity of the beam current of 50 μA, before increasing again due to the secondary electron emission induced by the electron beam. Note that the I_{beam} current in the figure includes both the beam current $I_{\mathrm{EB},T}$ and the resulting secondary and backscattered electron emission $I_{\mathrm{SEE},B,\mathrm{eb}}$, that is, $I_{\mathrm{beam}} = I_{\mathrm{EB},T} + I_{\mathrm{SEE},B,\mathrm{eb}}$. Because of the maximum secondary electron yield of $Y_{\max} = 2 \cdot 0.97$ used here, the total current is even more positive than without electron impact. Progressing to the right in the figure, the total current is affected by the secondary electron yield as well as the properties of the ambient plasma electrons and ions. At about 0 V, the total current drops quickly, because the photoelectrons and secondary electrons are attracted back to the positively charged spacecraft. This drop in current at 0 V explains the threshold of electron beam current required for the onset of charging. For the target spacecraft, a higher electron beam current essentially shifts the total current curve downward. The total current line is nearly vertical at 0 V, so if the equilibrium potential is about 0 V, it barely changes with the increasing or decreasing electron beam current. Once the chosen electron beam current exceeds a certain threshold (in Fig. 4 about 20 μA more, so a total of 70 μA), the total current line crosses 0 μA to the left of the vertical drop at 0 V, and the target charges negatively. Similar observations can be made for the servicing spacecraft, where a certain electron beam current is required in order to charge the servicer positively (for the servicer, the total current curve shifts upward with increasing electron beam current).

The effect of different beam currents on the equilibrium potential of the target is shown in Fig. 5. The equilibrium potentials are again marked with circles. The plasma parameters used here are $n_e = 0.95\ \mathrm{cm}^{-3}$, $T_e = 1400$ eV, $n_i = 0.75\ \mathrm{cm}^{-3}$, and $T_i = 7100$ eV. A beam energy of 20 keV is chosen, and the servicer and target spacecraft radii are $R_S = 1$ m and $R_T = 1$, respectively. Two different cases are considered. In one case, both the servicer and target are in sunlight (indicated by S). In the other case, the servicer is in sunlight but eclipses the target (indicated by E). Looking first at the sunlight cases (solid lines), the equilibrium potential is approximately zero for most beam currents. Only a beam current of 85 μA is strong enough to charge the target negatively in sunlight. For an eclipsed target, the natural potential (zero electron beam current) is also close to zero for the given plasma properties. Increasing the beam current drastically affects the potential of the target in eclipse, with equilibria of about −16 kV for 10 μA, −13 kV for 50 μA, and −10 kV for 85 μA. Notice that, for the given selection of beam currents, the equilibrium potential is more negative for a smaller beam current of 10 μA than for 85 μA. This relatively unintuitive effect is due the charging of the servicer. For a stronger beam current, the servicer charges more positively, thus decreasing the energy of the electron beam as it reaches the target and limiting the most negative possible potential of the target.

The secondary electron emission plays an important role in spacecraft charging. To generalize the idea of the secondary electron yield, the charged particle yield (CPY) is introduced, defined as

$$\mathrm{CPY}(\phi_T) = \frac{I_{\mathrm{tot},T}(\phi_T)}{I_{\mathrm{EB}}} + 1 \tag{17}$$

That is, the CPY represents the number of outgoing electrons (and incoming ions) per incoming beam electron. For CPY = 1, the system is at equilibrium. Similarly to the secondary electron yield (SEY), the CPY is shown as a function of the effective energy $E_{\mathrm{eff}} = E_{\mathrm{EB}} - \phi_S + \phi_T$ of the beam in Fig. 6a. The SEY used in this work is represented by the black line. If the system consisted solely of the electron beam hitting the target and the resulting secondary electron emission, this would also correspond to the CPY. The CPY for the 50 and 85 μA cases (both in sunlight S and eclipse E) from Fig. 5 are shown again for a beam energy of 20 keV in red and additionally for 30 keV in blue. As discussed in the Introduction, the x-ray and secondary electron methods for remotely estimating electric potential yield more information in certain ranges of effective energies. For the x-ray method, higher effective energies are preferred because more elements of the surface can be identified while sensing the potential. For the secondary electron method, lower effective energies are preferred due to the higher secondary electron emission in this energy range, resulting in a better signal. Thus, plotting the CPY as a function of the effective energy quickly illustrates which sensing method is better suited for a given charging scenario. In the figure, the CPY = 1 line is represented by the black dash-dotted line, and the effective energy for the equilibria of the various cases is indicated by the dash-dotted line in the corresponding color.

Figure 6b shows the dynamic charging behavior for the parameters from Fig. 6a. Starting at the natural potential of close to 0 V (no electron beam), the electron beam is turned on to charge both spacecraft. The lines approach the equilibrium effective energy on the horizontal axis and the equilibrium target potential on the vertical axis, and markers are placed at time steps of 10 ms to illustrate the time scale. The shape and orientation of the trajectories indicates whether or not the servicer is charging. If the line is horizontal, only the servicer is charging, and the effective energy is decreasing until

Downloaded by Univ of Colorado Libraries - Boulder on October 8, 2024 | http://arc.aiaa.org | DOI: 10.2514/1.A36010

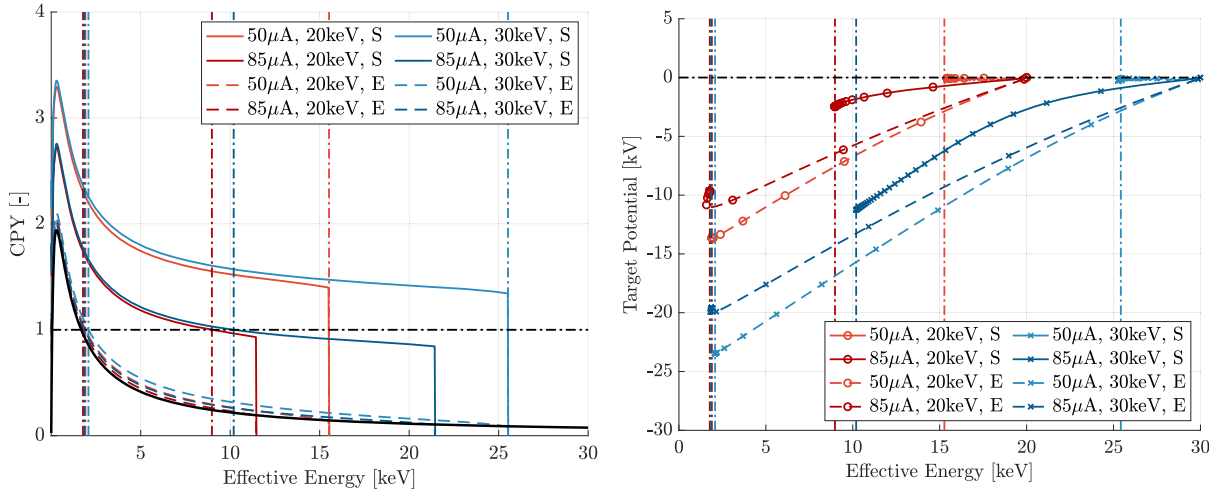

a) Charged particle yield **b) Transients**

Fig. 6 Charging as function of effective energy.

the servicer has reached its equilibrium. If the line is straight but with a downward trend, only the target is charging, and a curve indicates that both spacecraft are charging at that moment. For an electron beam current of 50 μA in sunlight, only the servicer charges, while the target remains at approximately 0 V. In all other cases, both spacecraft are charging at the beginning, but the servicer reaches its equilibrium potential first. This plot illustrates nicely the effect of changing the electron beam energy. Increasing the electron beam energy by 10 keV essentially shifts the lines 10 keV to the right. If this barely changes the equilibrium potential of the servicer, then the charging trajectory intersects the line of the equilibrium effective energy approximately 10 kV lower than for the less energetic beam, resulting in a target equilibrium potential that is 10 kV more negative than before.

III. Multiple Equilibria

A. Overview

Under specific circumstances, the secondary electron emission due to electron beam impact can cause multiple equilibria to exist. This is also indirectly shown in Ref. [7] chap. 9, but not in detail, and any other currents besides electron-beam-induced currents are neglected. Multiple equilibria for spacecraft charging are known to exist for double-Maxwellian plasma as discussed in Ref. [7] chap. 5, but have not been recognized for single-Maxwellian plasma. For example, multiple equilibria due to electron beam impact exist for the case of 50 μA in eclipse in Fig. 5 and are highlighted in Fig. 7. As discussed in Sec. II.A, the equilibrium potential corresponds to the potential for which the total current is equal to zero. This occurs three times in Fig. 7 for the given charging model. There is a significant jump in current at the potential at which the electron beam is not energetic enough to reach the target, at about −15.5 kV in the figure (the servicer potential in this figure is +4.5 kV, and the beam energy is 20 keV). If the total current is positive without the electron beam hitting the target, but smaller in magnitude than the electron beam current, then there is a zero crossing at this potential, corresponding to an equilibrium (×). Because of the secondary electron emission, which is especially high for effective energies below approximately 1–2 keV, the total current increases again with increasing potential, resulting in another zero crossing and equilibrium (Δ). With increasing potential (increasing effective energy of the electron beam electrons), the secondary electron emission weakens, resulting in another equilibrium potential where the total current is zero (○). The left- and right-side equilibria are stable, while the center equilibrium is unstable. For a slight negative deviation of the potential from the center equilibrium, the current is negative, so the potential drifts farther away from the equilibrium. Similarly, for a slight deviation of the potential in the positive direction, the current is positive. Thus, the

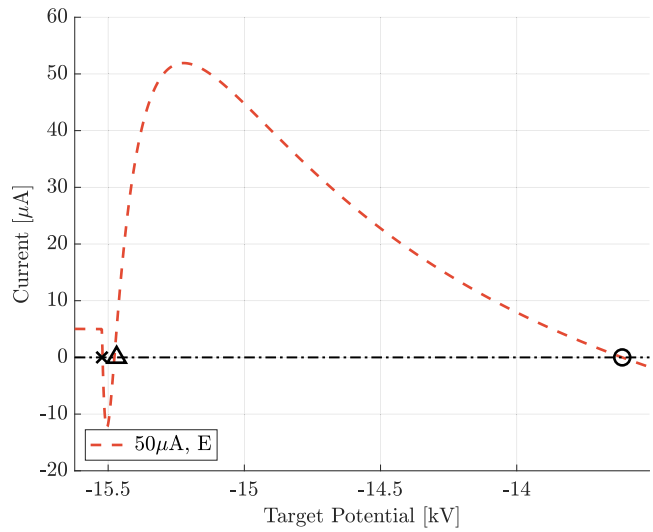

Fig. 7 Multiple equilibria: left and right equilibria are stable, and center equilibrium is unstable.

center equilibrium represents a divergence point. For multiple equilibria to exist, the conditions

$$I_{\mathrm{EB}} > I_{\mathrm{tot},T}(\phi_T = \phi_S - E_{\mathrm{EB}}, \phi_S) \tag{18a}$$

$$Y_{\mathrm{SEE},B,\mathrm{eb,max}} > 1 - \frac{I_{\mathrm{tot},T}(\phi_T = \phi_S - E_{\mathrm{EB}} + E_{\max}, \phi_S)}{I_{\mathrm{EB}}} \tag{18b}$$

must be fulfilled. If the first condition is not fulfilled, the beam current is not strong enough to dominate the natural current from the space environment, and only the right-side equilibrium exists. Without the second condition, the secondary electron emission is not significant enough, and only the left-side equilibrium exists. In either edge case, the center equilibrium aligns with either the right or left equilibrium.

Note that Fig. 7 only shows the total current for one specific servicer potential, i.e., for the servicer equilibrium potential of +4.5 kV. For a different servicer potential, the total current on the target shifts, and so do the equilibria of the target. This is due to the coupling effect of the electron beam, as the potential difference between the two spacecraft can only be as high as the energy of the electron gun. For example, the currents in Fig. 4 are computed for a servicer potential of +4.5 kV. If the servicer potential were +5.5 kV, the electron-beam-induced currents on the target would

Downloaded by Univ of Colorado Libraries - Boulder on October 8, 2024 | http://arc.aiaa.org | DOI: 10.2514/1.A36010

Downloaded by Univ of Colorado Libraries - Boulder on October 8, 2024 | http://arc.aiaa.org | DOI: 10.2514/1.A36010

shift by 1 kV to the right, also affecting the total current. Thus, some of the equilibria in Fig. 7 may not be achievable unless the servicer maintains a potential of +4.5 kV.

Figure 8 shows the time responses of the target potential (Fig. 8a) and servicer potential (Fig. 8b) for the same charging scenario as in Fig. 7 and for several initial conditions. The initial servicer potentials are 0, 1.5, 3, 4.5, and 6 kV and are indicated by the color of the lines. For each initial servicer potential, 50 initial target potentials are linearly spaced between −25 and −10 kV. As visible in the figures, both the target and servicer converge to different equilibrium potentials. One set of equilibria corresponds to the right-side target equilibrium: due to electron beam emission, the servicer charges to +4.5 kV, while the target charges to about −13.5 kV due to the electron beam impact and the resulting secondary electron emission. For the other set of equilibria, the servicer converges to about 0 V, and the target converges to about −20 kV. This corresponds to the case where the electron beam is initially unable to reach the target and comes back to the servicer. This causes the target to charge in the positive direction and to converge to a left-side equilibrium, i.e., the most negative potential possible for a given electron beam energy. The servicer converges to its natural potential, as the returning electron beam results in a net-zero beam-induced current.

For some initial conditions with the target starting between about −20 and −15 kV, the target initially charges positively but then charges negatively after some time and ends up at the equilibrium of −20 kV. This behavior can be explained in the following way. Initially, the beam is not able to reach the target and comes back to the servicer. Consequently, due to the net-zero beam-induced current on both spacecraft, the target and servicer are slowly decharging to their natural potential of about 0 V, so the target charges in the positive direction, while the servicer charges in the negative direction. This decreases the potential difference between the two spacecraft. After some time, the potential difference is small enough for the beam to hit the target. Once the beam hits the target, the target charges negatively and converges to −20 kV. As the beam is just barely able to reach the target and leave the servicer [modeled with the exponential dropoff in Eq. (13)], the servicer keeps charging negatively and converges to 0 V.

B. Change of Equilibrium

As shown previously, which equilibrium the target and servicer spacecraft settle to depends on the initial potential of both the servicer and the target and whether or not the beam is initially energetic enough to reach the target. However, this leaves the questions of how to get to a state where the beam is unable to reach the target in the first place and what could cause a jump from one equilibrium to another.

One way of changing the type of equilibrium (left side vs right side) is to simply vary the electron beam energy, as illustrated in Fig. 9 for the same charging environment as in Fig. 7. In this simulation, the servicer potential is held at 0 V. This makes the illustration simpler by eliminating the effect of the servicer potential on the charging response of the target. Figure 9a shows the response of the target potential over time as the beam energy is changed, while Fig. 9b

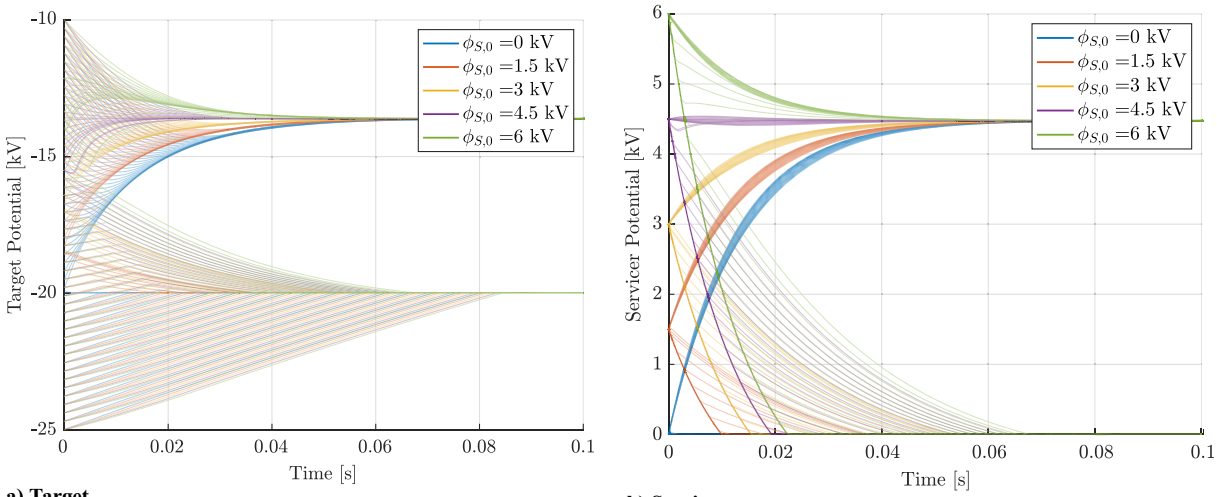

a) Target b) Servicer

Fig. 8 Multiple equilibria transients for various initial servicer potentials $\phi_{S,0}$.

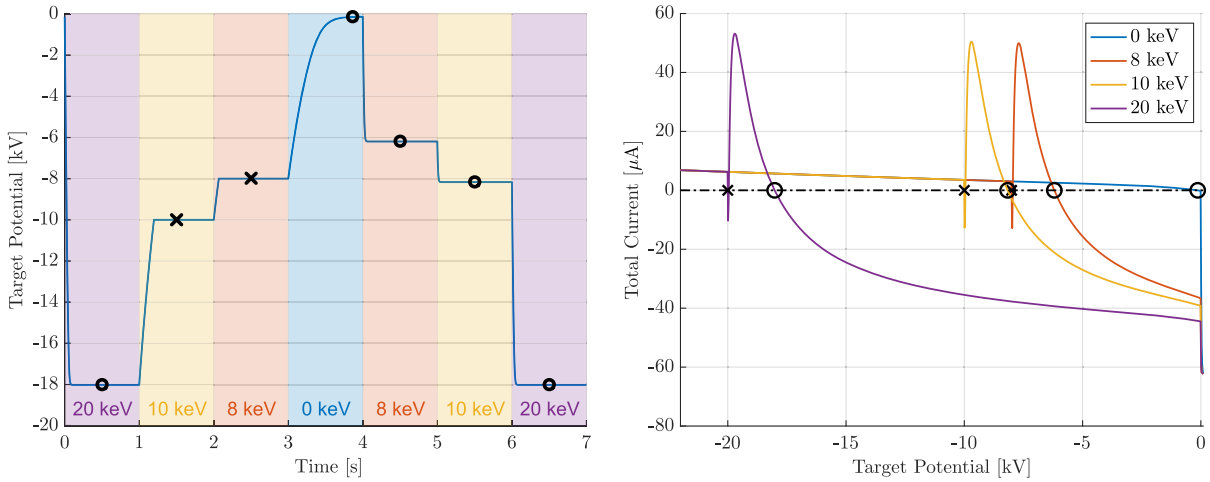

a) Transients b) Currents

Fig. 9 Change of equilibria due to electron beam energy variation. $I_{EB} = 50\ \mu$A.

Downloaded by Univ of Colorado Libraries - Boulder on October 8, 2024 | http://arc.aiaa.org | DOI: 10.2514/1.A36010

shows the total current on the target for each beam energy as a function of target potential. The left-side equilibria are indicated by ×, and the right-side equilibria are indicated by ○. The target starts at the natural potential of about 0 V. When hit by a 20 keV electron beam, the potential quickly changes to about −18 kV, corresponding to the right-side equilibrium. When the electron beam energy is changed to 10 keV, the potential converges to −10 kV, corresponding to the left-side equilibrium for this beam energy. That is, the equilibrium switched from the right side to the left side (although, for different beam settings) because the electron beam is initially unable to reach the target once the beam energy is reduced from 20 to 10 keV. Similar observations are made when changing the beam energy from 10 to 8 keV. When the electron gun is turned off (0 keV), there is only one possible equilibrium, that is, the natural potential of the target. Now, if the beam energy is increased, the right-side equilibrium is achieved for every beam energy. To reach a left-side equilibrium again, the beam energy needs to be reduced such that the beam is initially unable to reach the target. Figure 9a clearly illustrates that the same charging environment and beam settings (e.g., 10 keV) can result in two different final potentials depending on the initial conditions. Note that the time it takes the electron gun to adjust its beam energy is neglected here. That is, it is assumed that the beam energy changes faster than the spacecraft charge.

Varying the electron beam energy is a controlled (intentional) way of switching between left- and right-side equilibria. However, a switch of equilibria could also occur naturally. For a rotating (nonspherical) spacecraft, the sunlit area changes over time, and consequently the photoelectric current changes. If the resulting change in current is significant enough, the requirement for multiple equilibria in Eq. (18a) may not be fulfilled anymore. As a result, only the right-side equilibrium exists, causing a jump to that potential. This is illustrated in Fig. 10. Figure 10a shows the response of the target potential over time as the sunlit area of the target changes, while Fig. 10b shows the total current on the target for each fraction of sunlit area as a function of target potential. The servicer is assumed to be either fully eclipsed or fully sunlit. Again, the left-side equilibria are indicated by ×, and the right-side equilibria are indicated by ○.

Starting at a potential of −22 kV with both spacecraft in eclipse (0% sunlit area), the target potential converges to the left-side equilibrium of −20 kV. After 1 s, both spacecraft exit eclipse, with the servicer being entirely sunlit, while only 12.5% of the nominal photoelectric current area $A_{\mathrm{ph},0}$ of the target is sunlit. The resulting transients are interesting. If the entire electron beam escapes the servicer, the servicer charges to about +4.5 kV; if the entire beam comes back to the servicer, the servicer remains at about 0 V. Yet, the servicer converges to about 0.7 kV, and the target converges to −19.3 kV. This is one of the cases from Sec. II.B in which the target potential influences the charging of the servicer (as the target is highly charged). The increase in photoelectric current from 0 to 12.5% results in an increase in total current on the target that is constant over all negative potentials [Eq. (10)], essentially shifting the total current line in Fig. 10b upward. This upward shift causes the leftmost zero crossing to shift slightly to the right and consequently the left-side target equilibrium to shift a few volts in the positive direction. This allows the servicer to charge a bit more positively, as the potential difference between the two spacecraft can only be as high as the electron beam energy (without the presence of a charged target spacecraft, the servicer would charge to +4.5 kV). In turn, due to the limitation on the potential difference, the increased positive potential of the servicer causes the target potential to shift in the positive direction. This continues until the servicer and target potentials converge to 0.7 and −19.3 kV, respectively. This highlights one of the limitations of the assumption that the target potential does not influence whether or not the beam is able to leave the servicer as discussed in Sec. II.B. With the root-finding procedure highlighted in Sec. II.A, these (left-side) equilibrium potentials cannot be found. A more complex, bivariate root-finding algorithm is needed. Instead of solving for the equilibrium potential of the servicer and target sequentially, both equilibria must be computed simultaneously. At equilibrium, the current on both spacecraft must be zero, so the one-dimensional function

$$I_{\mathrm{sum}}(\phi_T, \phi_S) = \sqrt{I_{\mathrm{tot},T}(\phi_T, \phi_S)^2 + I_{\mathrm{tot},S}(\phi_T, \phi_S)^2} \tag{19}$$

is used to represent the sum of both currents. This current sum is shown in Fig. 11 as a function of the two spacecraft potentials, with the corresponding right-side and left-side equilibria highlighted. Using this

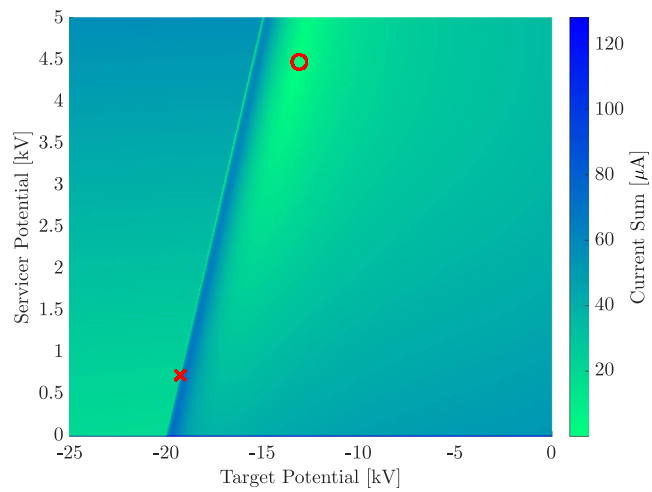

Fig. 11 Current sum for bivariate root-finding. $I_{\mathrm{EB}} = 50\ \mu$A, $E_{\mathrm{EB}} = 20$ keV.

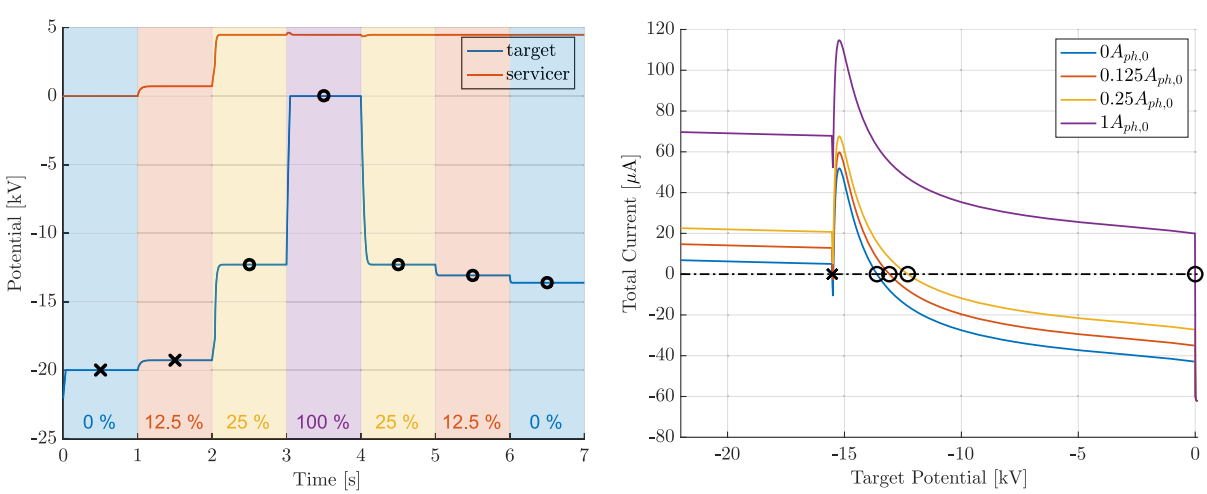

a) Transients **b) Total current on target (servicer at 4.5 kV)**

Fig. 10 Change of equilibria due to sunlight variation. $I_{\mathrm{EB}} = 50\ \mu$A.

Downloaded by Univ of Colorado Libraries - Boulder on October 8, 2024 | http://arc.aiaa.org | DOI: 10.2514/1.A36010

function, one can use a bivariate root finder to compute the potentials of both spacecraft simultaneously in a case where the more complex left-side equilibrium is of interest. For the case where the beam is initially energetic enough to reach the target, resulting in the right-side equilibrium, the root-finding procedure from Sec. II.A can be used.

As the sunlit area of the target increases to 25% of the nominally sunlit area $A_{\mathrm{ph},0}$, the target potential jumps from the left-side equilibrium to the right-side one. In fact, the left-side equilibrium disappears: the increase in photoelectric current shifts the total current line in Fig. 10b so far upward that the requirement in Eq. (18a) for the left-side equilibrium is not fulfilled anymore. That is, the electron beam current is not significant enough for the given space environment such that the left-side equilibrium can exist. As a result of the jump to the right-side equilibrium, the servicer converges to the corresponding equilibrium at +4.5 kV. With an increase to 100% of the nominally sunlit area $A_{\mathrm{ph},0}$ of the target, the target potential converges to about 0 V; that is, the electron beam current is not strong enough to charge the target at all for the given space environment. Any subsequent variations in the sunlit area cause the equilibrium potential of the target to change, but the potential remains at the right-side equilibrium, even when both spacecraft are eclipsed again. To achieve a left-side equilibrium again, another variation needs to be included, such as a change in the electron beam energy.

Note that the two ways of changing the type of equilibrium (left side vs right side) presented here are fundamentally different. One way, by changing the electron beam energy, puts the current target potential into a different region of convergence by essentially shifting the total current line left or right. In this way, one can change the type of equilibrium in both directions: from left-side equilibrium to the right side, and vice versa. This way of changing the type of equilibrium can also be achieved by varying the potential of the servicer using some additional current such as, for example, an extra electron or ion beam that is uncoupled from the target by facing in the other direction. The other way, by changing the target spacecraft orientation and the resulting photoelectric current, removes the left-side equilibrium and thereby enforces the right-side equilibrium, by essentially shifting the total current line upward. In this way, however, one can change the type of equilibrium only in one direction: from left to right. To go back to the left-side equilibrium, one needs to change another charging source, such as the electron beam energy. Any current fluctuations (change in plasma environment, variations in electron beam current, etc.), if significant enough, can cause the left-side equilibrium to disappear and consequently a jump to the right-side equilibrium [Eq. (18a)].

C. Significance and Potential Applications

As shown in this section, changes in the charging environment can cause a jump from one type of equilibrium to another, such as from the right-side equilibrium to the left-side one. If the charging environment allows for multiple equilibria and the electron beam energy is reduced by several kilo-electron-volts (corresponding to approximately the difference in kilovolts between the left- and right-side equilibria), the potential of the target may converge to the left-side equilibrium. Not only is this an unexpected charging behavior, but it also affects the remote sensing of the electric potential. For the left-side equilibrium, the impact energy of the electron beam on the target is close to zero, and barely any secondary electrons or x-rays are excited, which is needed for the electric potential sensing methods.

From a charge control perspective, where the potentials of the servicer and target are controlled by adjusting the electron beam current and energy, the left-side equilibrium provides a new control algorithm. Instead of implementing a closed-loop control that uses feedback of the potential of the servicer and target to control the beam parameters accordingly, the beam energy is reduced to make sure a left-side equilibrium is obtained. The value of that equilibrium potential is approximately $\phi_T \approx \phi_S - E_{\mathrm{EB}}$, so as long as the potential of the servicer is measured, no estimation of the target potential is required. One drawback of this open-loop control is that no secondary electrons or x-rays are excited. This results in a similar signal as if the beam does not hit the target at all, so it cannot be verified if the electron beam is charging the target at all, unless the x-rays and secondary electrons excited by the ambient plasma are used to passively estimate the potential [31]. The other drawback is that the left-side equilibrium results in a low servicer potential. For the electrostatic tractor, high-magnitude potentials with opposing signs are desired for both spacecraft to maximize the attractive electrostatic force between the two vehicles. To achieve a more positive servicer potential, an additional electron beam can be used that is uncoupled from the target by facing in the other direction.

These findings are also important when using numeric root finders to compute the equilibrium potential. If the rightmost equilibrium is of interest (as in this work), then the limits for the root-finding algorithm are set to only accept an equilibrium potential greater than $\phi_T \geq \phi_S - E_{\mathrm{EB}} + E_{\max}$, where $E_{\max}$ is the effective energy where the maximum secondary electron yield occurs. This limit ensures that the two equilibria to the left are ignored. However, for a small enough maximum secondary electron yield, the rightmost equilibrium and the unstable equilibrium may not exist. Moreover, a more complex bivariate root-finding algorithm may be required as opposed to the sequential root-finding approach used in this work.

Future work may look into the dynamic effects of the jump between equilibria on electric potential sensing and control methods and how this affects the reorbit process with the electrostatic tractor. The challenges and benefits of the aforementioned open-loop charge control approach may also be investigated further. Multiple equilibria also exist in double-Maxwellian plasma [7], motivating a potential study about the similarities between electron-beam-induced and plasma-induced multiple equilibria.

IV. Study of Electron Beam Effects Around Earth and Moon

Using the charging model from Sec. II.A and the findings from Sec. III, the equilibrium potentials induced by the electron beam are studied in GEO and cislunar space. Only right-side equilibria are considered, so the bounds for the numerical root finder are set accordingly as described in Sec. III.C. The left-side equilibrium is achieved if the beam is initially not energetic enough to reach the target, due to a large potential difference between servicer and target or a reduction in electron beam energy. Thus, the right-side equilibrium is generally more likely when starting from natural potentials, which motivates the focus on it within this study.

A. Geostationary Earth Orbit

The plasma environment data for GEO are taken from Ref. [40], which provides the electron and ion temperature and density (T_e, n_e, T_i, n_i) as a function of local time and Planetary K-index (Kp index). The data come from averaging in-orbit measurements from satellites flown by the Los Alamos National Laboratory between 1990 and 2001. Local time represents the location in GEO, where a local time of 1200 h indicates that the spacecraft is between sun and Earth and a local time of 0000 h corresponds to the spacecraft being behind Earth. The Kp index characterizes the intensity of geomagnetic storms. Thus, the plasma parameters are a function of the local time and Kp index. While the servicer is assumed to always be in sunlight in GEO, two cases are considered for the target: either the target is also in sunlight or it is eclipsed by the servicer (resulting in no photoelectric current on the target).

Figure 12 shows the equilibrium potential of the servicer and target as a function of electron beam current, for several Kp indices and a beam energy of 20 keV. The shaded regions represent the various local times for each Kp index; that is, these regions are bounded by the minimum and maximum equilibrium potential across all local times obtained for a given beam current and Kp index. The solid lines indicate that the target is in sunlight, while the dashed lines indicate that the target is eclipsed by the servicer. The servicer equilibrium potential increases approximately linearly with increasing beam current. It takes some minimum current for the servicer to charge. This can be explained with Fig. 4 (note that this figure shows the currents on the target, but the currents on the servicer are similar despite the beam currents of the opposite sign). At 0 V, there is a

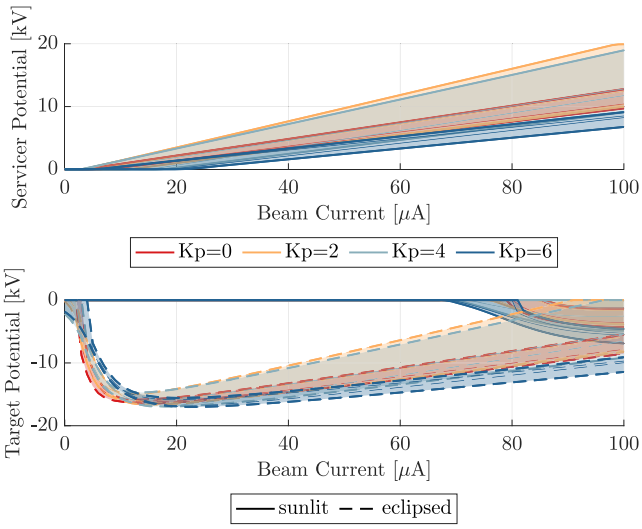

Fig. 12 Equilibrium potential vs electron beam current in GEO. $E_{EB} = 20$ keV.

significant current dropoff because the secondary electron and photoelectric currents reduce exponentially with increasing positive potential. Thus, it requires some minimal current to overcome this dropoff. This is provided by the electron beam current, which essentially shifts the total current upward for the servicer. Similarly to the servicer, it takes some minimal current to charge the target negatively. This can also be explained using Fig. 4, but in this case, the total current is shifted downward by the electron beam on the target. For the eclipsed target, the equilibrium potential is up to a few kilovolts negative even without the electron beam (0 μA). With increasing beam current, the equilibrium potential increases quickly in the negative direction before approaching 0 V again, approximately linearly. This is interesting as one might expect that a higher beam current results in a more negative target potential. However, the electron beam couples the charging of the servicer and target. With increasing beam current, the servicer charges more positively, and less energy of the electron beam is left to charge the target [15,16]. While a higher Kp index is associated with more negative charging due to more energetic electrons at increased geomagnetic activity, the Kp indices of 2 and 4 show less negative charging than a Kp index of 0. This is due to a decreased electron density for Kp indices between 2 and 5 in the data. Consequently, the servicer charges more positively, and less energy is left to charge the target.

As a satellite orbits around Earth in GEO, it moves through various plasma environments throughout the day, specified by the local time. Figure 13 shows the equilibrium potential of the servicer and target as a function of local time, for several beam currents. The shaded regions represent the various Kp indices; that is, these regions are bounded by the minimum and maximum equilibrium potential across all Kp indices obtained for a given local time and beam current. In Fig. 13a, both spacecraft are in sunlight, and high beam currents between 60 and 90 μA are used. The natural potential (zero beam current) of both the servicer and target is a few volts positive across all local times. In the dawn and dusk hours, the target charges the most negatively, while the servicer charges the most positively a little after noon. Most natural charging is negative and occurs in the dawn and dusk hours (see Ref. [7] chap. 1). The electron-beam-induced potentials follow the same trend. Note that the equilibrium potential of the servicer varies more than 15 kV throughout the day for the same beam parameters. These differences in charging during one day affect the electrostatic force between the two spacecraft and can consequently impact the performance of the multimonth reorbit process of the electrostatic tractor debris removal method. With the servicer in sunlight and the target eclipsed by the servicer, only small beam currents are needed to significantly charge the target, as the natural potential of the eclipsed spacecraft can already be a few kilovolts, as shown in Fig. 13b. The trends throughout the day are similar to when the target is in sunlight, with small differences due to the weaker electron beam current.

The significant charging levels of the eclipsed target for small beam currents of only a few microamperes raise the question of how much this influences the remote sensing methods. For these methods, it is desired to measure the electric potential without significantly changing the potential during the estimation process. Figure 14 shows the maximum current that is allowed to not change the

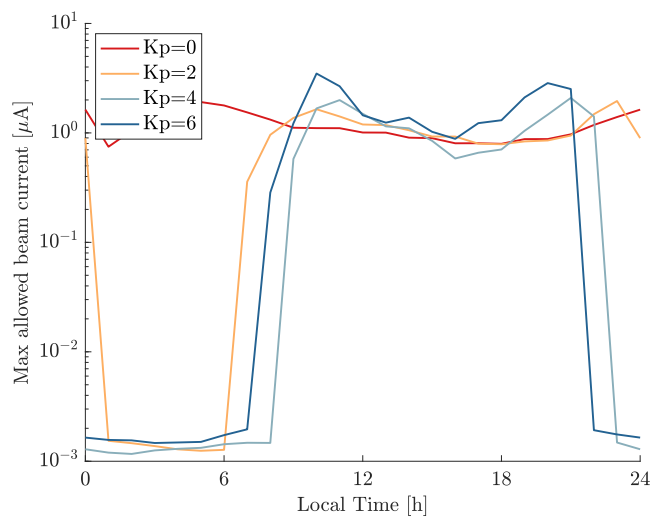

Fig. 14 Maximum allowed current in GEO eclipse.

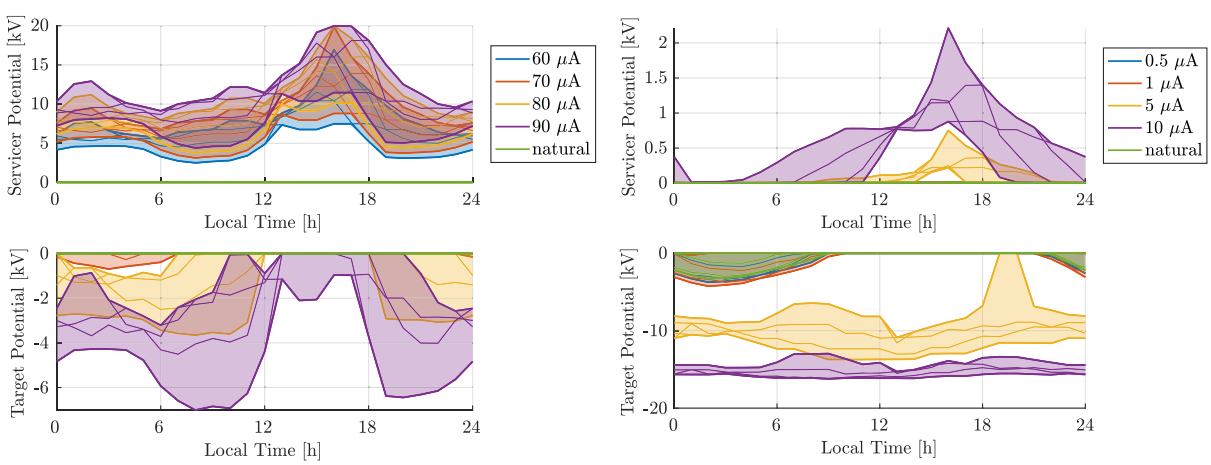

a) Sunlight **b) Eclipse**

Fig. 13 Equilibrium potential vs GEO local time. $E_{EB} = 20$ keV.

Downloaded by Univ of Colorado Libraries - Boulder on October 8, 2024 | http://arc.aiaa.org | DOI: 10.2514/1.A36010

Downloaded by Univ of Colorado Libraries - Boulder on October 8, 2024 | http://arc.aiaa.org | DOI: 10.2514/1.A36010

potential of the target by more than 1 V from its equilibrium, as a function of GEO local time and for various Kp indices. For a Kp index of 0, the maximum allowed current is a few microamperes for all local times. For higher geomagnetic activity, the maximum allowed current drops to only a few nanoamperes for the night-side local times. Such low currents may not be feasible for the electron gun used by the servicing satellite. Instead, one could quickly pulse the electron beam to reduce the average current and let the target object periodically recharge to its natural potential. Note that such a low current also affects the signal strength for the sensing methods, as a low current results in fewer secondary electrons and x-rays to be generated. However, because the beam is pulsed at a known frequency, one can strengthen the signal using a bandpass filter. The charging dynamics of a pulsed beam and the potential benefits of pulsing for electric potential sensing and control will be investigated in future work.

B. Lunar Orbit

Another region with high spacecraft charging levels is cislunar space. As the Moon orbits Earth, it moves through different regions of Earth's magnetic field and into the solar wind. Thus, for spacecraft charging considerations, four regimes are defined for cislunar space according to the NASA Design Specification For Natural Environments (DSNE) [41]: the plasma sheet, the magnetotail lobes, the magnetosheath, and the solar wind. The DSNE provides the electron and ion temperature and density as well as the ion bulk velocity $v_{i,\mathrm{bulk}}$ for these cislunar environment regimes. In the magnetosheath and solar wind, a plasma wake with a depletion of plasma density forms on the downwind side of the Moon because the Moon obstructs the flowing solar wind [42–44]. Thus, the plasma data for the magnetosheath and solar wind regions is given separately for the day side (D) and wake side (W) of the Moon. In addition, the data are altitude dependent in the magnetosheath wake-side and solar wind wake-side regions, with three altitude ranges for the magnetosheath (100–2000, 2000–12,000, and above 12,000 km) and four for the solar wind (100–500, 500–2000, 2000–12,000, and above 12,000 km). This results in a total of 11 different cislunar regions for spacecraft charging. The DSNE provides the mean and maximum for the plasma data, but only the mean is used here. In this work, it is assumed that both spacecraft are eclipsed in the magnetosheath and solar wind wake-side regions. In the day-side regions, the servicer is always assumed to be in sunlight, and the target is either in sunlight or eclipsed by the servicer.

Figure 15 shows the equilibrium potential of the servicer and target as a function of electron beam current for the various cislunar regions and a beam energy of 20 keV. The shaded regions represent the various altitudes; that is, these regions are bounded by the minimum and maximum equilibrium potential across all altitudes obtained for a given beam current and cislunar region. The charging behavior in the plasma sheet and magnetotail lobes is similar to GEO, with beam currents of about 70 μA required for the onset of charging if the target is in sunlight and with a maximum target potential magnitude for a beam current of about 10 μA if the target is eclipsed. The charging behavior for a sunlit target is also similar in the magnetosheath and solar wind day-side regions, although the target is charging to more negative potentials. This is due to the higher electron density in these regions, causing the servicer to barely charge positively and leaving more electron beam energy to charge the target. Another reason for the higher charging levels of the target is that the bulk velocity $v_{i,\mathrm{bulk}}$ of the ions with respect to the spacecraft is greater than the thermal velocity w_i of the ions in these regions, in which case the third case in Eq. (2) is applied. Consequently, the ion-induced secondary electron emission is reduced, allowing for more negative target potentials. Because of the servicer potential being close to neutral in the magnetosheath and solar wind day-side regions, the equilibrium potentials for an eclipsed target are highly negative for beam currents above approximately 5 μA, without a steady increase in potential with increasing beam current. In the magnetosheath and solar wind wake-side regions, where both the servicer and target are eclipsed, the charging levels of the target are altitude dependent due to the plasma data being provided for different altitude regions. For lower altitudes, the ion bulk velocity is less than the ion thermal velocity, and the maximum potential magnitude is around 10 μA, similar to an eclipsed target in the plasma sheet or magnetotail lobes. For higher altitudes, the ion bulk velocity is greater than the ion thermal velocity, and the equilibrium potential is highly negative for most beam currents, similar to an eclipsed target in the magnetosheath and solar wind day-side regions.

To highlight the impact of an electron beam on the remote sensing methods, the maximum current that is allowed to not change the potential of the target by more than 1 V from its equilibrium is illustrated in Fig. 16 for the cislunar regions. The figure shows the four cislunar regimes (plasma sheet, magnetotail lobes, magnetosheath, and solar wind) and an indicator of the maximum allowed current for each of the 11 regions. Green indicates that more than 1 μA beam current is required to change the potential by more than 1 V from its equilibrium, yellow corresponds to 0.1 to 1 μA, and red highlights that a beam current of less than 0.1 A disturbs the potential by more than 1 V. A white edge of the circle corresponds to the target being in sunlight, while a gray edge corresponds to an eclipsed target. Additionally, the regions are highlighted where the bulk velocity $v_{i,\mathrm{bulk}}$ of the ions with respect to the spacecraft is greater than the thermal velocity w_i of the ions [in which case the third case in Eq. (2) is applied for ram-side charging]. In the plasma sheet and magnetotail, the

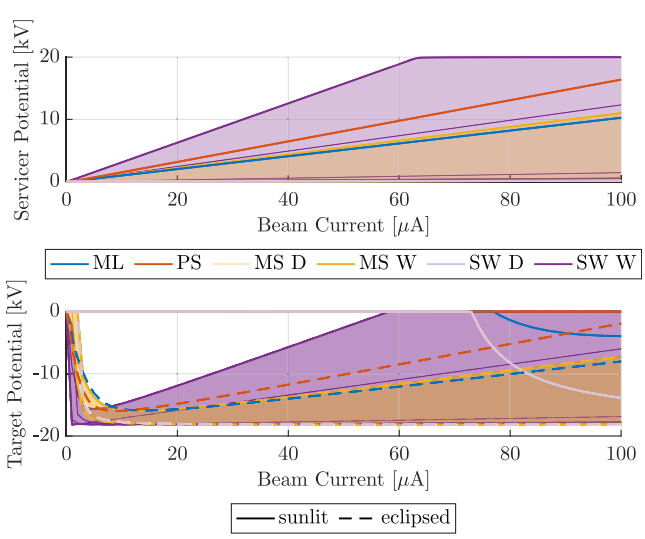

Fig. 15 Equilibrium potential vs electron beam current in cislunar space. $E_{\mathrm{EB}} = 20$ keV.

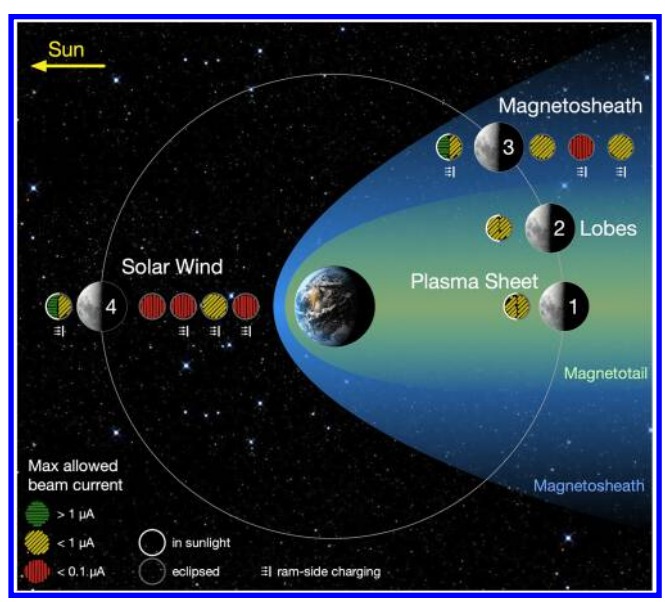

Fig. 16 Maximum allowed current in cislunar space.

maximum allowed current is between 0.1 and 1 μA, regardless of whether or not the target is eclipsed. In the magnetosheath and solar wind day-side regions, higher beam currents are allowed when the target is in sunlight, and only lower beam currents are allowed when the target is eclipsed. In the magnetosheath and solar wind wake-side regions, the maximum allowed current is generally low and mostly less than 0.1 μA. This aligns with the higher charging levels of spacecraft in these regions. It was found that the maximum allowed current is mostly higher when the natural equilibrium potential is a few volts positive, or when the electron population is dense and low energy, causing a larger gradient of the plasma electron current at slightly negative potentials, which in turn results in a lower sensitivity of the potential to the total current. High sensitivity of the equilibrium potential to the beam current is possible when the natural equilibrium is very close to a turning point of the current (where the charging equations switch from one case to another, for example, at 0 V).

V. Conclusions

This paper investigates the effect of electron emission and impact on the spacecraft charging levels of two neighboring spacecraft. For this analysis, an electron gun is assumed to be mounted on a servicing satellite and aimed at a target satellite, resulting in electron beam emission on the servicer and electron beam impact on the target. The electron beam is only energetic enough to reach the target if the initial beam energy is greater than the potential difference between the two spacecraft. Otherwise, the beam is attracted back to the servicer, resulting in a net zero beam current on both the servicer and target. This relationship between the beam energy and the electric potentials of the spacecraft leads to a coupling of charging dynamics between the servicer and target.

Multiple electric potential equilibria are found to exist for the servicer and target in a single-Maxwellian plasma. This is due to the emission of secondary electrons that are excited by the electron beam impacting on the target and due to the energy-potential relation of the electron beam. The existence of multiple equilibria depends on the magnitude of the beam current relative to the currents induced by the space environment as well as the secondary electron yield of the surface material of the target. Moving from one stable equilibrium to another is possible due to a fast decrease in beam energy or increase in servicer potential; or due to current fluctuations caused by a rotating spacecraft (resulting in a time-varying photoelectric current), changes in beam current or the plasma environment. These findings are important for active charging and remote electric potential sensing methods that use an electron beam. Potential applications that use the knowledge about multiple equilibria include an open-loop charge controller that takes advantage of the stability of the most negative equilibrium potential of the target.

Finally, the spacecraft charging levels due to the electron beam are studied in geostationary Earth orbit and cislunar space, and the effect of the electron beam on remote electric potential sensing methods is investigated. It is found that, especially when the target is eclipsed, the electron beam may significantly divert the electric potential of the target from its natural equilibrium while the potential is measured.

Acknowledgments

The authors would like to thank Kaylee Champion for her assistance with the SIMION simulations and the detailed review of this paper and Amy Haft for her contributions to the study of multiple equilibria. This work was supported by the U.S. Air Force Office of Scientific Research under grants FA9550-20-1-0025 and FA9550-23-1-0570. Julian Hammerl gratefully acknowledges funding from the NASA FINESST fellowship (award number 80NSSC22 K1849).

References

[1] Katz, I., Davis, V., and Snyder, D., "Mechanism for Spacecraft Charging Initiated Destruction of Solar Arrays in GEO," *36th AIAA Aerospace Sciences Meeting and Exhibit*, AIAA Paper 1998-1002, 1998. https://doi.org/10.2514/6.1998-1002

[2] Brandhorst, H., and Rodiek, J., "Improving Space Utilization by Increasing Solar Array Reliability," *AIAA SPACE 2007 Conference and Exposition*, AIAA Paper 2007-6024, 2007. https://doi.org/10.2514/6.2007-6024

[3] Wilson, K., and Schaub, H., "Impact of Electrostatic Perturbations on Proximity Operations in High Earth Orbits," *Journal of Spacecraft and Rockets*, Vol. 58, No. 5, 2021, pp. 1293–1302. https://doi.org/10.2514/1.A35039

[4] Schaub, H., and Moorer, D. F., "Geosynchronous Large Debris Reorbiter: Challenges and Prospects," *Journal of the Astronautical Sciences*, Vol. 59, Nos. 1–2, 2012, pp. 161–176. https://doi.org/10.1007/s40295-013-0011-8

[5] Bengtson, M., Wilson, K., Hughes, J., and Schaub, H., "Survey of the Electrostatic Tractor Research for Reorbiting Passive GEO Space Objects," *Astrodynamics*, Vol. 2, No. 4, 2018, pp. 291–305. https://doi.org/10.1007/s42064-018-0030-0

[6] Olsen, R. C., "Record Charging Events from Applied Technology Satellite 6," *Journal of Spacecraft and Rockets*, Vol. 24, No. 4, 1987, pp. 362–366. https://doi.org/10.2514/3.25925

[7] Lai, S. T., *Fundamentals of Spacecraft Charging*, Princeton Univ. Press, Princeton, NJ, 2011. https://doi.org/10.2307/j.ctvcm4j2n

[8] Garrett, H. B., and Whittlesey, A. C., *Guide to Mitigating Spacecraft Charging Effects*, Wiley, Hoboken, NJ, 2012, Chap. 3. https://doi.org/10.1002/9781118241400

[9] Mandell, M., Davis, V., Cooke, D., Wheelock, A., and Roth, C., "Nascap-2k Spacecraft Charging Code Overview," *IEEE Transactions on Plasma Science*, Vol. 34, No. 5, 2006, pp. 2084–2093. https://doi.org/10.1109/TPS.2006.881934

[10] Ferguson, D. C., Murray-Krezan, J., Barton, D. A., Dennison, J. R., and Gregory, S. A., "Feasibility of Detecting Spacecraft Charging and Arcing by Remote Sensing," *Journal of Spacecraft and Rockets*, Vol. 51, No. 6, 2014, pp. 1907–1913. https://doi.org/10.2514/1.A32958

[11] Lundgreen, P., and Dennison, J. R., "Strategies for Determining Electron Yield Material Parameters for Spacecraft Charge Modeling," *Space Weather*, Vol. 18, No. 4, 2020, pp. 1–13. https://doi.org/10.1029/2019SW002346

[12] Hastings, D. E., "A Review of Plasma Interactions with Spacecraft in Low Earth Orbit," *Journal of Geophysical Research: Space Physics*, Vol. 100, No. A8, 1995, pp. 14,457–14,483. https://doi.org/10.1029/94 JA03358

[13] Matéo-Vélez, J.-C., Theillaumas, B., Sévoz, M., Andersson, B., Nilsson, T., Sarrailh, P., Thiébault, B., Jeanty-Ruard, B., Rodgers, D., Balcon, N., and Payan, D., "Simulation and Analysis of Spacecraft Charging Using SPIS and NASCAP/GEO," *IEEE Transactions on Plasma Science*, Vol. 43, No. 9, 2015, pp. 2808–2816. https://doi.org/10.1109/TPS.2015.2447523

[14] Parker, L. N., Minow, J., and Blackwell, W., Jr., "Analysis of Lunar Surface Charging for a Candidate Spacecraft Using NASCAP-2 K," *10th Spacecraft Charging Technology Conference*, Centre national d'´ etudes spatiales (CNES), Paris, France, 2007, pp. 1–11.

[15] Schaub, H., and Sternovsky, Z., "Active Space Debris Charging for Contactless Electrostatic Disposal Maneuvers," *Advances in Space Research*, Vol. 53, No. 1, 2014, pp. 110–118. https://doi.org/10.1016/j.asr.2013.10.003

[16] Hogan, E. A., and Schaub, H., "Impacts of Hot Space Plasma and Ion Beam Emission on Electrostatic Tractor Performance," *IEEE Transactions on Plasma Science*, Vol. 43, No. 9, 2015, pp. 3115–3129. https://doi.org/10.1109/TPS.2015.2451001

[17] Hogan, E. A., and Schaub, H., "Impacts of Tug and Debris Sizes on Electrostatic Tractor Charging Performance," *Advances in Space Research*, Vol. 55, No. 2, 2015, pp. 630–638. https://doi.org/10.1016/j.asr.2014.10.023

[18] Hughes, J. A., and Schaub, H., "Electrostatic Tractor Analysis Using a Measured Flux Model," *Journal of Spacecraft and Rockets*, Vol. 57, No. 2, 2020, pp. 207–216. https://doi.org/10.2514/1.A34359

[19] Wilson, K., Romero-Calvo, Á., and Schaub, H., "Constrained Guidance for Spacecraft Proximity Operations Under Electrostatic Perturbations," *Journal of Spacecraft and Rockets*, Vol. 59, No. 4, 2022, pp. 1304–1316. https://doi.org/10.2514/1.A35162

[20] Hammerl, J., and Schaub, H., "Effects of Electric Potential Uncertainty on Electrostatic Tractor Relative Motion Control Equilibria," *Journal of Spacecraft and Rockets*, Vol. 59, No. 2, 2022, pp. 552–562. https://doi.org/10.2514/1.A35165

[21] Bengtson, M., Hughes, J., and Schaub, H., "Prospects and Challenges for Touchless Sensing of Spacecraft Electrostatic Potential Using

Downloaded by Univ of Colorado Libraries - Boulder on October 8, 2024 | http://arc.aiaa.org | DOI: 10.2514/1.A36010

Electrons," *IEEE Transactions on Plasma Science*, Vol. 47, No. 8, 2019, pp. 3673–3681.
https://doi.org/10.1109/TPS.2019.2912057

[22] Wilson, K., and Schaub, H., "X-Ray Spectroscopy for Electrostatic Potential and Material Determination of Space Objects," *IEEE Transactions on Plasma Science*, Vol. 47, No. 8, 2019, pp. 3858–3866.
https://doi.org/10.1109/TPS.2019.2910576

[23] Brace, L. H., "Langmuir Probe Measurements in the Ionosphere," *Geophysical Monograph-American Geophysical Union*, Vol. 102, Jan. 1998, pp. 23–36.
https://doi.org/10.1029/GM102p0023

[24] Lai, S. T., and Miller, C., "Retarding Potential Analyzer: Principles, Designs, and Space Applications," *AIP Advances*, Vol. 10, No. 9, 2020, Paper 095324.
https://doi.org/10.1063/5.0014266

[25] Bengtson, M. T., Wilson, K. T., and Schaub, H., "Experimental Results of Electron Method for Remote Spacecraft Charge Sensing," *Space Weather*, Vol. 18, No. 3, 2020, pp. 1–12.
https://doi.org/10.1029/2019SW002341

[26] Wilson, K. T., Bengtson, M. T., and Schaub, H., "X-Ray Spectroscopic Determination of Electrostatic Potential and Material Composition for Spacecraft: Experimental Results," *Space Weather*, Vol. 18, No. 4, 2020, pp. 1–10.
https://doi.org/10.1029/2019SW002342

[27] Wilson, K., Romero-Calvo, Á., Bengtson, M., Hammerl, J., Maxwell, J., and Schaub, H., "Development and Characterization of the ECLIPS Space Environments Simulation Facility," *Acta Astronautica*, Vol. 194, May 2022, pp. 48–58.
https://doi.org/10.1016/j.actaastro.2021.12.037

[28] Hammerl, J., Romero-Calvo, Á., López, A., and Schaub, H., "Touchless Potential Sensing of Complex Differentially-Charged Shapes Using X-Rays," *Proceedings of the AIAA SciTech 2022 Forum and Exposition*, AIAA Paper 2022-2312, 2022.
https://doi.org/10.2514/6.2022-2312

[29] Reimer, L., *Scanning Electron Microscopy*, 2nd ed., Springer Series in Optical Sciences, Springer–Verlag, Berlin, 1998, Chap. 10.
https://doi.org/10.1007/978-3-540-38967-5

[30] Romero-Calvo, Á., Hammerl, J., and Schaub, H., "Touchless Potential Sensing of Differentially Charged Spacecraft Using Secondary Electrons," *Journal of Spacecraft and Rockets*, Vol. 59, No. 5, 2022, pp. 1623–1633.
https://doi.org/10.2514/1.A35355

[31] Wilson, K., Hammerl, J., and Schaub, H., "Using Plasma-Induced X-Ray Emission to Estimate Electrostatic Potentials on Nearby Space Objects," *Journal of Spacecraft and Rockets*, Vol. 59, No. 4, 2022, pp. 1402–1405.
https://doi.org/10.2514/1.A35161

[32] Pisacane, V. L., *The Space Environment and Its Effects on Space Systems*, AIAA, Reston, VA, 2008.
https://doi.org/10.2514/4.862533

[33] Hippler, R., Pfau, S., Schmidt, M., and Schoenbach, K. H., *Low Temperature Plasma Physics: Fundamental Aspects and Applications*, 1st ed., Wiley, Hoboken, NJ, 2001.

[34] Jahn, J. M., Goldstein, J., Reeves, G. D., Fernandes, P. A., Skoug, R. M., Larsen, B. A., and Spence, H. E., "The Warm Plasma Composition in the Inner Magnetosphere During 2012–2015," *Journal of Geophysical Research: Space Physics*, Vol. 122, No. 11, 2017, pp. 11,018–11,043.
https://doi.org/10.1002/2017 JA024183

[35] Davis, V. A., and Mandell, M. J., "NASCAP-2 K Version 4.3 Scientific Documentation," U.S. Air Force Research Lab. TR AFRL-RV-PS-TR-2017-0001, 2016.

[36] Draine, B. T., and Salpeter, E. E., "On the Physics of Dust Grains in Hot Gas," *Astrophysical Journal*, Vol. 231, July 1979, pp. 77–94.
https://doi.org/10.1086/157165

[37] Sternovsky, Z., Chamberlin, P., Horanyi, M., Robertson, S., and Wang, X., "Variability of the Lunar Photoelectron Sheath and Dust Mobility Due to Solar Activity," *Journal of Geophysical Research: Space Physics*, Vol. 113, No. 10, 2008, pp. 18–21.
https://doi.org/10.1029/2008 JA013487

[38] Romero-Calvo, Á., Cano-Gómez, G., and Schaub, H., "Simulation and Uncertainty Quantification of Electron Beams in Active Spacecraft Charging Scenarios," *Journal of Spacecraft and Rockets*, Vol. 59, No. 3, 2022, pp. 739–750.
https://doi.org/10.2514/1.A35190

[39] Hughes, J., and Schaub, H., "Prospects of Using a Pulsed Electrostatic Tractor with Nominal Geosynchronous Conditions," *IEEE Transactions on Plasma Science*, Vol. 45, No. 8, 2017, pp. 1887–1897.

[40] Denton, M. H., Thomsen, M. F., Korth, H., Lynch, S., Zhang, J. C., and Liemohn, M. W., "Bulk Plasma Properties at Geosynchronous Orbit," *Journal of Geophysical Research: Space Physics*, Vol. 110, No. A7, 2005.
https://doi.org/10.1029/2004 JA010861

[41] Roberts, B. C., "SLS-SPEC-159: Cross-Program Design Specification for Natural Environments (DSNE)," NASA Marshall Space Flight Center TR SLS-SPEC-159, Revision G, 2019, https://ntrs.nasa.gov/citations/20200000867 [retrieved 25 June 2024].

[42] Halekas, J. S., Bale, S. D., Mitchell, D. L., and Lin, R. P., "Electrons and Magnetic Fields in the Lunar Plasma Wake," *Journal of Geophysical Research: Space Physics*, Vol. 110, No. A7, 2005.
https://doi.org/10.1029/2004 JA010991

[43] Ness, N. F., "Interaction of the Solar Wind with the Moon," *Solar-Terrestrial Physics/1970: Part II*, Springer–Verlag, Dordrecht, The Netherlands, 1972, pp. 159–205.
https://doi.org/10.1007/978-94-009-3693-5_21

[44] Schubert, G., and Lichtenstein, B. R., "Observations of Moon-Plasma Interactions by Orbital and Surface Experiments," *Reviews of Geophysics*, Vol. 12, No. 4, 1974, p. 592.
https://doi.org/10.1029/RG012i004p00592

L. N. Parker
Associate Editor

Downloaded by Univ of Colorado Libraries - Boulder on October 8, 2024 | http://arc.aiaa.org | DOI: 10.2514/1.A36010